

NUMERICAL ANALYSIS OF NEWTONIAN AND NON-NEWTONIAN  
LID-DRIVEN CAVITY FLOW IN PLANE AND CURVED GEOMETRIES

by

Hatice Mercan

B.S., in M.E., Yıldız Technical University , 2003

Submitted to the Institute for Graduate Studies in  
Science and Engineering in partial fulfillment of  
the requirements for the degree of  
Master of Science

Graduate Program in Mechanical Engineering  
Boğaziçi University

2006

NUMERICAL ANALYSIS OF NEWTONIAN AND NON-NEWTONIAN  
LID-DRIVEN CAVITY FLOW IN PLANE AND CURVED GEOMETRIES

APPROVED BY:

Asst. Prof. Kunt Atalık .....  
(Thesis Supervisor)

Assoc. Prof. Osman Börekçi .....

Asst. Prof. Ali Ecder .....

DATE OF APPROVAL: 16.02.2006

## ACKNOWLEDGEMENTS

I would like to first thank to my advisor Asst. Professor Kunt Atalık. I was fortunate to work with him. His academic vision, advice, guidance, motivation and support made this thesis possible.

Thanks to each of my friends for all their support. There are too many names and for the fear of leaving one out accidentally I will not try. I just want you all know that I cherish our friendships.

Finally, I would especially like to thank to my family; babacım, annecim, Yavuz abi, Oya abla and Fatih abi for everything.

This thesis has been supported by Boğaziçi University Scientific Research Project BAP05HA602.

## ABSTRACT

# NUMERICAL ANALYSIS OF NEWTONIAN AND NON-NEWTONIAN LID-DRIVEN CAVITY FLOW IN PLANE AND CURVED GEOMETRIES

The aim of this thesis is to develop a numerical solution to the lid driven cavity problem in plane and curved geometries for both Newtonian and non-Newtonian fluids. The planar case is the lid-driven square cavity problem and the curved cases are the lid-driven polar cavity and the lid-driven arc-shaped cavity problems. For the non-Newtonian case, inelastic Power-Law fluid model is adopted. The study is carried out in terms of investigating the inertia effects on the flow field as well as the shear-thickening and/or shear-thinning attributes of the fluid. The inertia effects are characterized by the non-dimensional Reynolds number, whereas non-Newtonian effects such as shear thinning and shear thickening are characterized by Power-Law Reynolds number and Power-Law indices.

## ÖZET

### NEWTONYEN ve NEWTONYEN OLMAYAN AKIŞKANLARIN KAPAK TAHRİKLİ OYUK AKIŞLARININ DÜZLEMSEL VE EĞRİSEL GEOMETRİLER İÇİN SAYISAL ANALİZİ

Bu tezin amacı, Newtonyen ve Newtonyen olmayan akışkanların kapak tahrikli oyuk akışlarının düzlemsel ve eğrisel geometrilerde sayısal çözümlerinin geliştirilmesidir. Düzlemsel geometri kare, eğrisel geometriler ise kutupsal ve yay şekilli oyuk olarak seçilmiştir. Newtonyen olmayan akış modeli için Üssel Kanun ile tanımlı elastik olmayan bir bünye denklemi kullanılmıştır. Çalışmada eylemsizlik kuvvetlerinin etkisinin yanı sıra akışkanda kayma incelmesi ve/veya kayma kalınlaşması etkileri incelenmiştir. Eylemsizlik etkileri boyutsuz Reynolds sayısı ile, kayma incelmesi ve kayma kalınlaşması gibi Newtonyen olmayan etkiler ise Üssel Kanun Reynolds sayısı ve Üssel Kanun endisleriyle karakterize edilmiştir.

## TABLE OF CONTENTS

ACKNOWLEDGEMENTS . . . . .	iii
ABSTRACT . . . . .	iv
ÖZET . . . . .	v
LIST OF FIGURES . . . . .	vii
LIST OF TABLES . . . . .	x
LIST OF SYMBOLS/ABBREVIATIONS . . . . .	xi
1. INTRODUCTION . . . . .	1
2. MATHEMATICAL MODELING . . . . .	5
2.1. Governing Equations for Incompressible Newtonian Fluid Flow in Rectangular Coordinates . . . . .	5
2.2. Governing Equations for Incompressible Newtonian Fluid Flow in Curvilinear Coordinates . . . . .	9
2.3. Governing Equations for Non–Newtonian Fluid Flow in Rectangular Coordinates . . . . .	10
2.4. Governing Equations for Non–Newtonian Fluid Flow in Curvilinear Coordinates . . . . .	13
3. NUMERICAL METHOD . . . . .	15
3.1. Grid Generation . . . . .	15
3.1.1. Grid Generation Equations . . . . .	16
3.1.2. Grid Generation for Cavity Problems . . . . .	23
3.2. Discretization of Partial Differential Equations . . . . .	25
3.2.1. Time Integration Algorithm . . . . .	28
3.2.2. Space Integration Algorithm . . . . .	30
3.3. Code Validation . . . . .	32
4. RESULTS . . . . .	38
5. CONCLUSIONS . . . . .	59
APPENDIX A: TRANSFORMATIONS . . . . .	61
REFERENCES . . . . .	65

## LIST OF FIGURES

Figure 1.1.	Cross section of a lubrication device showing the relative position of friction and upper plates . . . . .	1
Figure 1.2.	Flow pattern and recirculation zone of a single groove . . . . .	1
Figure 1.3.	Lid-driven boundary conditions with the basic features . . . . .	2
Figure 2.1.	Boundary integration . . . . .	8
Figure 3.1.	Transformation, map, or coordinate system . . . . .	16
Figure 3.2.	A grid . . . . .	17
Figure 3.3.	Physical model of polar cavity with a moving lid . . . . .	24
Figure 3.4.	Physical model of arc-shape cavity with a moving lid . . . . .	25
Figure 3.5.	Sample grids . . . . .	26
Figure 3.6.	Comparison of Newtonian results of square cavity for $Re = 100$ and $Re = 1000$ . . . . .	33
Figure 3.7.	Centerline U-velocity for Reynolds numbers 100 and 1000 . . . . .	34
Figure 3.8.	Comparison of Newtonian results of polar cavity for $Re = 60$ and $Re = 350$ . . . . .	35
Figure 3.9.	Comparison of Newtonian results of arc cavity for $Re = 100$ , $Re = 1000$ and $Re = 1500$ . . . . .	37

Figure 4.1.	Effects of Power-Law index $n$ on the stream line contours for $Re_{PL} = 100$ . . . . .	44
Figure 4.2.	Shear thinning effect of Power-Law index $n$ on the stream line contours for $Re_{PL} = 100$ . . . . .	45
Figure 4.3.	Effects of Power-Law index $n$ on the stream line contours for $Re_{PL} = 1000$ . . . . .	46
Figure 4.4.	Transient variation of the flow field for $Re_{PL} = 1000$ and $n = 1.5$ .	47
Figure 4.5.	Convergence plots for $Re_{PL} = 1000$ and $n = 1.5$ . . . . .	48
Figure 4.6.	Effects of Power-Law index $n$ on the stream line contours for $Re_{PL} = 100$ . . . . .	49
Figure 4.7.	Effects of Power-Law index $n$ on the stream line contours for $Re_{PL} = 1000$ . . . . .	50
Figure 4.8.	Directions of vortices for $Re_{PL} = 1000$ and $n = 1.2$ . . . . .	51
Figure 4.9.	Effects of Power-Law index $n$ on the stream line contours for $Re_{PL} = 1700$ . . . . .	52
Figure 4.10.	Effects of Power-Law index $n$ on the stream line contours for $Re_{PL} = 100$ . . . . .	53
Figure 4.11.	Effects of Power-Law index $n$ on the stream line contours for $Re_{PL} = 500$ . . . . .	54
Figure 4.12.	Effects of Power-Law index $n$ on the stream line contours for $Re_{PL} = 1000$ . . . . .	55



Figure 4.13. Time evolution of arc shape cavity for  $Re_{PL} = 1500$ ,  $n = 1.2$  . . . 56

Figure 4.14. Convergence plots for arc shape cavity,  $Re_{PL} = 1000$  and  $n = 1.2$  . 57

Figure 4.15. Effects of Power-Law index  $n$  on the streamline contours for  $Re_{PL} =$   
1500 . . . . . 58

## LIST OF TABLES

Table 3.1.	Explicit Adams-Bashforth Methods . . . . .	29
Table 3.2.	Strength and location of the centers of primary vortex for the lid-driven square cavity problem . . . . .	34
Table 3.3.	Strength of the maximum and minimum vortices for the lid-driven arc-shape cavity problem . . . . .	36
Table 4.1.	Strength of the maximum corner vortices for the lid-driven square cavity problem . . . . .	39
Table 4.2.	Strength of the maximum and minimum vortices for the lid-driven arc-shape cavity problem . . . . .	42

## LIST OF SYMBOLS/ABBREVIATIONS

$D$	Rate of Deformation Tensor
$I$	Identity Tensor
$I_2$	Second Invariant of Rate of Strain Tensor
$J$	Jacobian of Coordinate Transformation
$l$	Distance normal to the Wall
$L$	Characteristic Length
$n$	Power-Law Index
$N_x, N_y$	Number of Grid Points in $x$ and $y$ Directions
$p$	Pressure
$Re$	Reynolds Number
$Re_{PL}$	Power-Law Reynolds Number
$R_i$	Radius of Moving Lid for Polar Cavity
$R_o$	Outer Radius for Polar Cavity
$t$	Time
$t^*$	Dimensionless Time
$u, v$	Velocity Components in $x$ and $y$ Directions
$u_\infty$	Characteristic Velocity, Velocity of the Moving Lid
$x, y$	Rectangular Coordinates
$\alpha, \beta, \gamma$	Coordinate Transformation Metrics
$\theta$	Angle of Polar Cavity
$\kappa$	Fluid Consistency
$\mu$	Absolute Viscosity
$\mu_v$	Power-Law Viscosity Function
$\xi, \eta$	Body-Fitted Curvilinear Coordinates
$\rho$	Fluid Density
$\tau$	Stress Tensor
$\psi$	Stream Function
$\psi^*$	Dimensionless Stream Function

$\psi_l$	Stream Function Value at Distance $l$
$\psi_w$	Stream Function Value at Wall
$\Omega$	Vorticity
$\Omega^*$	Dimensionless Vorticity
$\Omega_l$	Vorticity Value at Distance $l$
$\Omega_w$	Vorticity Value at Wall
<i>FTCS</i>	Forward Time Centered Space
<i>REN</i>	Relative Error Norm
<i>SOR</i>	Successive Over Relaxation

## 1. INTRODUCTION

The problem of lid-driven flows in cavities has been an important subject for studies because of its fundamental nature and broad range of natural, industrial and biomedical applications. Understanding the physics of the inertia induced vortex flows is important for a number of engineering applications such as lubrication systems, collectors, evaporating sprays and flow channels. Figure 1.1 [1] shows a cross sectional view of a lubrication device having an upper moving plate and a friction layer, as well as their relative position during the continuously slipping mode. Figure 1.2 [1] shows the detail of the recirculation pattern in a single groove. The analysis of laminar flow in systems similar to lubrication devices has been the main focus of many researchers. The flow inside the groove can be modeled as a lid driven cavity flow with a top moving lid and stationary walls.

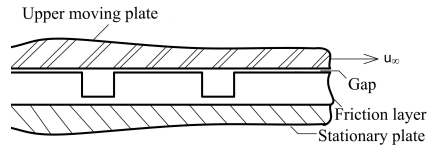


Figure 1.1. Cross section of a lubrication device showing the relative position of friction and upper plates

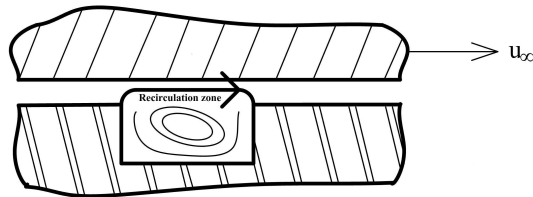


Figure 1.2. Flow pattern and recirculation zone of a single groove

The lid-driven cavity flow of a Newtonian fluid has been studied since the pioneering paper of Burggraf [2] back in 1966. The Newtonian flow of a fluid in square cavity with a moving lid is shown in Figure 1.3 with some basic features. Over the years the problem has spawned a huge number of studies. The new numerical schemes and the new representations of the governing flow equations have been tested with this classical problem because of its relatively easy boundary conditions and well known results [3], [4], [5], [6]. For the Newtonian square cavity Barragy & Carey have used a  $p$ -type finite element scheme with a refined element mesh. They have obtained a highly accurate solution for steady cavity flow [7].

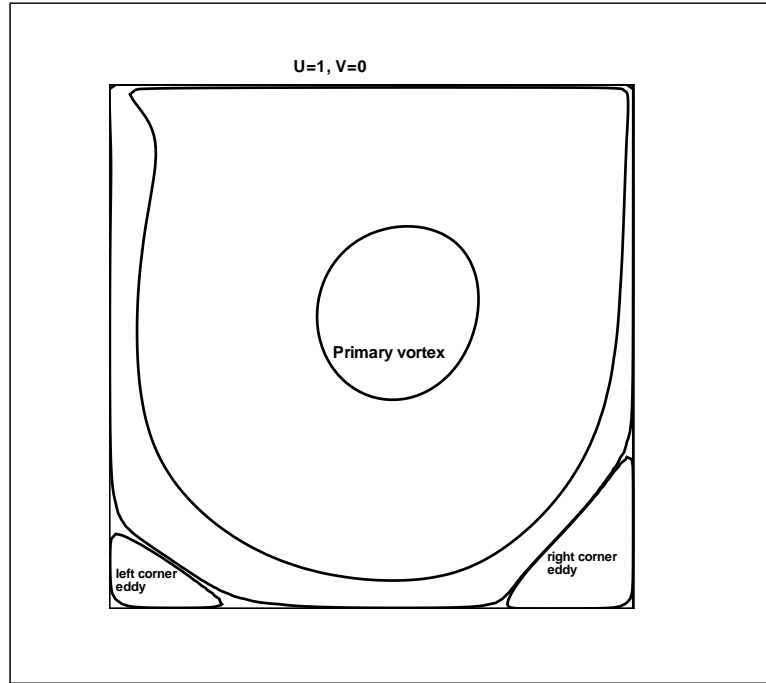


Figure 1.3. Lid-driven boundary conditions with the basic features of square cavity flow (*for Reynolds Number  $\leq 1000$* )

Botella & Peyret [3] have used a Chebyshev collocation method and also obtained highly accurate spectral solutions for the lid driven cavity flow.

Ghia *et.al.* [8] have applied a multi-grid strategy to the coupled strongly implicit method developed by Rubin & Khosla [9]. They have presented results for high Reynolds numbers with very fine grids.

Most of studies dealing with the numerical solution of the lid-driven cavity problem are concerned with the two dimensional problem in rectangles [4]. For example, studies of Ghia, *et.al.* [8] and Theodossiou & Sousa [10], are restricted to the analysis of the fluid motion in a rectangular cavity, and only a few reports deal with the cavity possessing an irregular shape. Furthermore, in other cases the configuration is simplified to a rectangular cavity even though it may not really be rectangular. For instance, the oil grooves installed in the friction material of the wet clutches are basically deformable and not perfectly rectangular; however, they are normally modeled to be rigid, rectangular channels with a moving lid by many authors [1], [11].

Recently Chen *et.al.* [12] have introduced a different geometry, an arc-shape cavity with a moving horizontal lid, and they have obtained results for different Reynolds numbers with an induced buoyancy. They used stream function-vorticity formulation for the solution of unsteady Navier–Stokes equations. The numerical scheme they have adopted is Successive Over Relaxation (SOR) for stream function equation and Forward Time Centered Space (FTCS) method for the time integration of vorticity transport equation.

Experimental and numerical results on the flow of viscoelastic fluids and fluids which can be modeled with Generalized Newtonian model flowing inside a rectangular cavity have been reported by some authors. Grillet & Shaqfeh [13], [14] have made an experimental investigation of the lid-driven flow of a Boger fluid and presented the numerical solution of the problem with a finite element simulation.

Bell & Surana [15] have presented a  $p$ -version least squares finite element formulation (LSFEF) for two dimensional, incompressible, non–Newtonian fluid flow under isothermal and non–isothermal conditions. For isothermal Power–Law model they obtained numerical results for lid-driven square cavity flow using different power–law indices.

For modeling the viscous non-Newtonian behaviour Neofytou [16] has employed the Power-Law, Quemada and the modified Bingham and Casson models. Using a

numerical scheme based on finite volume formulation he presented the non-Newtonian effects first by using different models and secondly by using shear thinning and shear thickening attributes of the fluid inside a lid driven square cavity.

In the present study stream function-vorticity formulation is used to solve numerically the lid driven cavity problem in plane and curved geometries for both Newtonian and non-Newtonian fluids. For the non-Newtonian case, inelastic Power-Law fluid model is applied. The numerical method that is used is an iterative method for the stream function formulation and an explicit time integration technique for the vorticity transport equation. For the validation of the numerical methods and the computational schemes the square, polar and arc cavity problems are utilized for various Reynolds ( $Re$ ) numbers and the results are compared with corresponding results available in the literature. The study is carried out in terms of investigating the inertia effects on the flow field as well as the shear-thickening and/or shear-thinning attributes of the fluid. The inertia effects are characterized by the non-dimensional Reynolds number, whereas non-Newtonian effects such as shear thinning and shear thickening are characterized by Power-Law Reynolds number and Power-Law indices.

It is expected to observe the above mentioned effects of inertia as well as shear thinning and shear thickening on the formation and growth of primary and secondary vortices in the cavities.

In Chapter 2 mathematical model of the problem is introduced. The governing flow equations for Newtonian and non-Newtonian cases are covered for both cartesian and curvilinear coordinates.

In Chapter 3 Numerical method is described. Elliptic grid generation technique is explained in detail and discretization of the partial differential equations is illustrated. Finally the comparison of the Newtonian results with the previous studies are presented to validate the accuracy of the numerical method. In the final chapter the results are shown and described in detail for square, polar and arc cavity geometries.



## 2. MATHEMATICAL MODELING

### 2.1. Governing Equations for Incompressible Newtonian Fluid Flow in Rectangular Coordinates

The fundamental equations of fluid motion in differential form are derived from:

- (1) Conservation of mass (continuity)
- (2) Conservation of linear momentum (Newton's second law)
- (3) Conservation of energy (first law of Thermodynamics)

The resulting system of equations in a differential form are known as the governing flow equations. In the isothermal case the third set of equations will drop.

For applications in which the density remains uniform throughout the domain, the assumption of incompressible flow is invoked. In general, in two dimensions, the governing equations for an incompressible, isothermal two dimensional flow may be expressed in two different formulations based on the dependent variables used. First is the primitive variable formulation expressed in terms of the pressure and velocity. The second form of the equations is the so-called vorticity–stream function equations which are derived from the Navier–Stokes equations by incorporating the definitions for the vorticity and the stream function.

In terms of horizontal and vertical velocity components  $u$ ,  $v$  where  $\mathbf{v} = (u, v, 0)$  the equations of continuity and conservation of momentum in Cartesian coordinates are

$$\frac{\partial u}{\partial x} + \frac{\partial v}{\partial y} = 0, \tag{2.1}$$

$$\rho \left( \frac{\partial u}{\partial t} + u \frac{\partial u}{\partial x} + v \frac{\partial u}{\partial y} \right) = \frac{\partial \tau_{xx}}{\partial x} + \frac{\partial \tau_{xy}}{\partial y}, \quad (2.2)$$

$$\rho \left( \frac{\partial v}{\partial t} + u \frac{\partial v}{\partial x} + v \frac{\partial v}{\partial y} \right) = \frac{\partial \tau_{yx}}{\partial x} + \frac{\partial \tau_{yy}}{\partial y}, \quad (2.3)$$

In Equation (2.2) and (2.3)  $\rho$  denotes the fluid density while  $\tau_{ij}$  refer to components of the stress tensor. For a Newtonian fluid the stress–rate of strain relation (i.e. constitutive equation) in tensor form is

$$\tau = -pI + 2\mu D, \quad (2.4)$$

where  $p$  is the pressure,  $\mu$  is the absolute viscosity,  $D$  is the rate of deformation tensor and  $I$  is the identity tensor.

When the Newtonian constitutive relation (2.4) is introduced in (2.2)–(2.3), the Navier–stokes equations in two dimensional Cartesian coordinates can be written as:

$$\rho \left( \frac{\partial u}{\partial t} + u \frac{\partial u}{\partial x} + v \frac{\partial u}{\partial y} \right) = -\frac{\partial p}{\partial x} + \mu \left( \frac{\partial^2 u}{\partial x^2} + \frac{\partial^2 u}{\partial y^2} \right) \quad (2.5)$$

$$\rho \left( \frac{\partial v}{\partial t} + u \frac{\partial v}{\partial x} + v \frac{\partial v}{\partial y} \right) = -\frac{\partial p}{\partial y} + \mu \left( \frac{\partial^2 v}{\partial x^2} + \frac{\partial^2 v}{\partial y^2} \right) \quad (2.6)$$

The set of three Equations (2.1), (2.5) and (2.6) in the three unknowns  $u$ ,  $v$ ,  $p$  can be reduced to a set of two equations by eliminating the pressure from (2.5) and (2.6). Introducing stream function ( $\psi$ ) and vorticity ( $\Omega$ ) defined by

$$\begin{aligned} u &= \frac{\partial \psi}{\partial y} & v &= -\frac{\partial \psi}{\partial x} \\ \Omega &= \frac{\partial v}{\partial x} - \frac{\partial u}{\partial y} \end{aligned} \quad (2.7)$$

then casts the equations in a stream function–vorticity formulation. All velocities are made dimensionless by choosing velocity of the lid in lid-driven cavity flow  $u_\infty$  as characteristic velocity and length of the moving lid in lid-driven cavity flow  $L$  as the characteristic length. The dimensional stream function and vorticity,  $\psi$  and  $\Omega$  are related to their dimensionless counterparts  $\psi^*$  and  $\Omega^*$  through  $\psi = \psi^*/(u_\infty L)$  and  $\Omega = \Omega^* L/u_\infty$ , where dimensional time  $t$  is related to dimensionless time  $t^*$  through  $t = t^* L/u_\infty$ . Thus in dimensionless form and in terms of stream function and vorticity the equations of motion are (dropping the asterisks for simplicity)

$$\frac{\partial \Omega}{\partial t} + \frac{\partial}{\partial x} (u\Omega) + \frac{\partial}{\partial y} (v\Omega) = \frac{1}{Re} \left( \frac{\partial^2 \Omega}{\partial x^2} + \frac{\partial^2 \Omega}{\partial y^2} \right) \quad (2.8)$$

$$\frac{\partial^2 \psi}{\partial x^2} + \frac{\partial^2 \psi}{\partial y^2} = -\Omega \quad (2.9)$$

where the Reynolds number  $Re$  is defined as

$$Re = \frac{\rho_\infty u_\infty L}{\mu_\infty} \quad (2.10)$$

and  $\rho_\infty$  is the fluid density,  $\mu_\infty$  is the viscosity,  $u_\infty$  is the characteristic velocity i.e. lid velocity in lid-driven cavity flow, and  $L$  is the characteristic length i.e. length of the moving lid in lid driven cavity flow.

In this study we shall use non-dimensional, conservative form of the Navier-Stokes equations in two space dimensions with stream function-vorticity formulation. One of the advantages of this formulation is that the pressure term does not appear explicitly in either of the equations. Therefore the system of equations is solved to provide the vorticity field. A major disadvantage of the formulation is in the direct extension to three dimensions. Furthermore, a difficulty associated with the formulation is due to lack of the boundary condition on vorticity. Therefore, numerical boundary conditions for the vorticity must be derived. The boundary conditions for lid-driven cavity flow is:

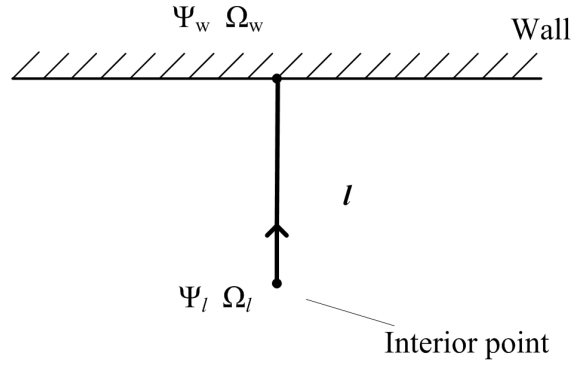


Figure 2.1. Boundary integration

$$u = 0, \quad v = 0, \quad \psi = 0, \quad \Omega_w = \left[ \frac{2(\psi_w - \psi_l)}{\Delta l^2} \right], \quad \text{on the stationary walls} \quad (2.11)$$

$$u = 1, \quad v = 0, \quad \psi = 0, \quad \Omega_w = \left[ \frac{2(\psi_w - \psi_l)}{\Delta l^2} - \frac{2u_\infty}{\Delta l} \right], \quad \text{on the moving lid surface} \quad (2.12)$$

where  $l$  is the distance normal to the wall,  $\Omega_w$  and  $\psi_w$  are values at the wall, and  $\Omega_l$  and  $\psi_l$  are values at an interior point situated at a distance  $l$  perpendicular to the wall as it is indicated in Figure 2.1 and finally  $u_\infty$  is the velocity of the moving lid in lid-driven cavity flow.

## 2.2. Governing Equations for Incompressible Newtonian Fluid Flow in Curvilinear Coordinates

For non-rectangular domains, it arises in all fields concerned with numerical solution of partial differential equations the need for accurate numerical representation of boundary conditions. Such representation is best accomplished when the boundary is such that it is coincident with some coordinate line, for then the boundary may be made to pass through the points of a finite difference grid constructed on the coordinate lines. Finite difference expression at, and adjacent to, the boundary may then be applied using only grid points on the intersection of coordinate lines without the need for any interpolation between points of the grid.

When we recast the governing flow equations, the vorticity–transport and stream function equations become in curvilinear coordinates:

$$\begin{aligned} \frac{\partial \Omega}{\partial t} + \frac{1}{J} \left[ \left( u \frac{\partial y}{\partial \eta} \frac{\partial \Omega}{\partial \xi} - u \frac{\partial y}{\partial \xi} \frac{\partial \Omega}{\partial \eta} \right) + \left( v \frac{\partial x}{\partial \xi} \frac{\partial \Omega}{\partial \eta} - v \frac{\partial x}{\partial \eta} \frac{\partial \Omega}{\partial \xi} \right) \right] \\ = \frac{1}{Re J^2} \left( \alpha \frac{\partial^2 \Omega}{\partial \xi^2} - 2\beta \frac{\partial^2 \Omega}{\partial \xi \partial \eta} + \gamma \frac{\partial^2 \Omega}{\partial \eta^2} \right) \end{aligned} \quad (2.13)$$

$$\alpha \frac{\partial^2 \psi}{\partial \eta^2} - 2\beta \frac{\partial^2 \psi}{\partial \xi \partial \eta} + \gamma \frac{\partial^2 \psi}{\partial \xi^2} = -J^2 \Omega \quad (2.14)$$

where  $\xi$  and  $\eta$  denote the components of transformed coordinate system,  $J$  is the transformation *Jacobian* and  $\alpha$ ,  $\beta$  and  $\gamma$  are the transformation metrics.

The boundary conditions can be specified in curvilinear coordinates [12]:

$$u = 0, \quad v = 0, \quad \psi = 0, \quad \Omega = -\frac{1}{J} \left( \frac{\partial y}{\partial \xi} \frac{\partial v}{\partial \eta} + u \frac{\partial x}{\partial \xi} \frac{\partial u}{\partial \eta} \right), \text{ on the stationary wall} \quad (2.15)$$

$$u = 1, \quad v = 0, \quad \psi = 0, \quad \Omega = -\frac{1}{J} \left( \frac{\partial x}{\partial \xi} \frac{\partial u}{\partial \eta} \right), \text{ on the moving lid surface} \quad (2.16)$$

### 2.3. Governing Equations for Non-Newtonian Fluid Flow in Rectangular Coordinates

Fluids for which stress and rate of strain are directly but non-linearly related to each other are called non-Newtonian fluids. For these fluids, the viscosity is no more constant but is a factor of rate of strain. Blood, mud, paints and polymers are some of the examples of non-Newtonian fluids. For inelastic non-Newtonian fluids one of the most common models is Power-Law model. For a power-law fluid the stress–rate of strain relation (or constitutive equation) in tensor form is [19]

$$\tau = -pI + 2\mu(D) D, \quad (2.17)$$

where  $p$  is the pressure,  $\mu$  is the viscosity function,  $D$  is the rate of deformation tensor and  $I$  is the identity tensor. Further,

$$\mu(D) = \mu_v = \kappa I_2^{\frac{n-1}{2}} \quad (2.18)$$

where  $\kappa$  is the fluid consistency,  $I_2$  is the second invariant of the rate-of-strain tensor  $D$  and  $n$  is the power-law index. For values of  $n$  between zero and unity the viscosity is shear thinning i.e. the apparent viscosity increases as strain rate increases, whereas for  $n > 1$  the viscosity is shear thickening i.e. the apparent viscosity decreases as strain rate increases and for  $n = 1$  Equation (2.17) reduces to constant Newtonian viscosity with  $\mu(D) = \mu$ .

For 2 –  $D$  flow the explicit form of  $I_2$  is given in rectangular coordinates by

$$I_2 = 2 \left( \frac{\partial u}{\partial x} \right)^2 + 2 \left( \frac{\partial v}{\partial y} \right)^2 + \left( \frac{\partial u}{\partial y} + \frac{\partial v}{\partial x} \right)^2 \quad (2.19)$$

Introducing Equation (2.17) in Equations (2.2), (2.3) and taking the derivatives with respect to  $y$  of the  $x$  component of momentum equation and with respect to  $x$  of the  $y$  component of momentum equation and subtracting the resulting equations from each other, we will get,

$$\begin{aligned} & \rho \left[ \frac{\partial}{\partial t} \left( \frac{\partial u}{\partial y} - \frac{\partial v}{\partial x} \right) + u \frac{\partial}{\partial x} \left( \frac{\partial u}{\partial y} - \frac{\partial v}{\partial x} \right) + v \frac{\partial}{\partial y} \left( \frac{\partial u}{\partial y} - \frac{\partial v}{\partial x} \right) + \left( \frac{\partial u}{\partial y} - \frac{\partial v}{\partial x} \right) \left( \frac{\partial u}{\partial x} + \frac{\partial v}{\partial y} \right) \right] = \\ & 2 \frac{\partial^2}{\partial x \partial y} (\mu_v) \left( \frac{\partial u}{\partial x} - \frac{\partial v}{\partial y} \right) - 2 \frac{\partial}{\partial x} (\mu_v) \left( \frac{\partial^2 v}{\partial y^2} + \frac{\partial^2 v}{\partial x^2} \right) + 2 \frac{\partial}{\partial y} (\mu_v) \left( \frac{\partial^2 u}{\partial y^2} + \frac{\partial^2 u}{\partial x^2} \right) + \\ & \mu_v \left( \frac{\partial^2}{\partial x^2} \left( \frac{\partial u}{\partial y} - \frac{\partial v}{\partial x} \right) + \frac{\partial^2}{\partial y^2} \left( \frac{\partial u}{\partial y} - \frac{\partial v}{\partial x} \right) \right) + \frac{\partial^2}{\partial y^2} (\mu_v) \left( \frac{\partial u}{\partial y} + \frac{\partial v}{\partial x} \right) - \frac{\partial^2}{\partial x^2} (\mu_v) \left( \frac{\partial u}{\partial y} + \frac{\partial v}{\partial x} \right) \end{aligned} \quad (2.20)$$

where  $\mu_v$  is the non-Newtonian viscosity for Power-Law model which is the function of second invariant of the rate of strain tensor as described in Equation (2.18). Introducing  $\mu_v$  and the first and second derivatives of  $\mu_v$  with respect to  $x$ ,  $y$  and  $\Omega = \frac{\partial v}{\partial x} - \frac{\partial u}{\partial y}$  the resulting vorticity-transport equation will be

$$\begin{aligned} \rho \left( \frac{\partial \Omega}{\partial t} + u \frac{\partial \Omega}{\partial x} + v \frac{\partial \Omega}{\partial y} \right) &= \kappa I_2^{\frac{n-1}{2}} \left( \frac{\partial^2 \Omega}{\partial x^2} + \frac{\partial^2 \Omega}{\partial y^2} \right) + \kappa \frac{(n-1)}{2} I_2^{\frac{n-3}{2}} \left( \frac{\partial I_2}{\partial y} \frac{\partial \Omega}{\partial y} + \frac{\partial I_2}{\partial x} \frac{\partial \Omega}{\partial x} \right) \\ &- \kappa \frac{(n-1)(n-3)}{2} I_2^{\frac{n-5}{2}} \left[ \left( \frac{\partial I_2}{\partial x} \frac{\partial u}{\partial x} + \frac{1}{2} \frac{\partial I_2}{\partial y} \left( \frac{\partial u}{\partial y} + \frac{\partial v}{\partial x} \right) \right) \frac{\partial I_2}{\partial y} \right] \\ &+ \kappa \frac{(n-1)(n-3)}{2} I_2^{\frac{n-5}{2}} \left[ \left( \frac{\partial I_2}{\partial y} \frac{\partial v}{\partial y} + \frac{1}{2} \frac{\partial I_2}{\partial x} \left( \frac{\partial u}{\partial y} + \frac{\partial v}{\partial x} \right) \right) \frac{\partial I_2}{\partial x} \right] \\ &- (n-1) I_2^{\frac{n-3}{2}} \left[ \frac{\partial}{\partial y} \left( \frac{\partial I_2}{\partial x} \frac{\partial u}{\partial x} + \frac{1}{2} \frac{\partial I_2}{\partial x} \left( \frac{\partial u}{\partial y} + \frac{\partial v}{\partial x} \right) \right) \right] \\ &+ (n-1) I_2^{\frac{n-3}{2}} \left[ \frac{\partial}{\partial x} \left( \frac{\partial I_2}{\partial y} \frac{\partial v}{\partial y} + \frac{1}{2} \frac{\partial I_2}{\partial x} \left( \frac{\partial u}{\partial y} + \frac{\partial v}{\partial x} \right) \right) \right] \end{aligned} \quad (2.21)$$

Then, all velocities are made dimensionless choosing  $u_\infty$ , velocity of the lid in lid-driven cavity flow, as characteristic velocity and choosing  $L$ , length of the moving lid in lid-driven cavity flow, as characteristic length. The dimensional stream function and vorticity,  $\psi$  and  $\Omega$  are related to their dimensionless counterparts  $\psi^*$  and

$\Omega^*$  through  $\psi = \psi^*/(u_\infty L)$  and  $\Omega = \Omega^* L/u_\infty$ , where dimensional time  $t$  is related to dimensionless time  $t^*$  through  $t = t^* L/u_\infty$ . Thus in dimensionless form and in terms of stream function and vorticity the equations of motion are (dropping the asterisks for simplicity):

$$\begin{aligned}
I_2^{\frac{n-1}{2}} \left( \frac{\partial^2 \Omega}{\partial x^2} + \frac{\partial^2 \Omega}{\partial y^2} \right) &+ \frac{(n-1)}{2} I_2^{\frac{n-3}{2}} \left( \frac{\partial I_2}{\partial y} \frac{\partial \Omega}{\partial y} + \frac{\partial I_2}{\partial x} \frac{\partial \Omega}{\partial x} \right) \\
&- \frac{(n-1)(n-3)}{2} I_2^{\frac{n-5}{2}} \left( G_1 \frac{\partial I_2}{\partial y} - G_2 \frac{\partial I_2}{\partial x} \right) \\
&- (n-1) I_2^{\frac{n-3}{2}} \left( \frac{\partial G_1}{\partial y} - \frac{\partial G_2}{\partial x} \right) = Re_{PL} \left( \frac{\partial \Omega}{\partial t} + u \frac{\partial \Omega}{\partial x} + v \frac{\partial \Omega}{\partial y} \right)
\end{aligned} \tag{2.22}$$

$$\frac{\partial^2 \psi}{\partial x^2} + \frac{\partial^2 \psi}{\partial y^2} = -\Omega \tag{2.23}$$

where

$$G_1 = \frac{\partial I_2}{\partial x} \frac{\partial u}{\partial x} + \frac{1}{2} \frac{\partial I_2}{\partial y} \left( \frac{\partial u}{\partial y} + \frac{\partial v}{\partial x} \right) \tag{2.24}$$

$$G_2 = \frac{\partial I_2}{\partial y} \frac{\partial v}{\partial y} + \frac{1}{2} \frac{\partial I_2}{\partial x} \left( \frac{\partial u}{\partial y} + \frac{\partial v}{\partial x} \right) \tag{2.25}$$

$$I_2 = 2 \left( \frac{\partial u}{\partial x} \right)^2 + 2 \left( \frac{\partial v}{\partial y} \right)^2 + \left( \frac{\partial u}{\partial y} + \frac{\partial v}{\partial x} \right)^2 \tag{2.26}$$

and the Reynolds number for Power-Law model,  $Re_{PL}$ , is defined by

$$Re_{PL} = \frac{\rho_\infty u_\infty^{(2-n)} L^n}{\kappa} \tag{2.27}$$



and  $\rho_\infty$  is the fluid density,  $u_\infty$  is the characteristic velocity i.e. lid velocity in lid-driven cavity flow,  $L$  is the characteristic length i.e. length of the moving lid in lid-driven cavity flow,  $\kappa$  denoting the consistency and  $n$  is the Power-Law index.

It is clear that when  $n = 1$  (the Newtonian case) Equations (2.22) and (2.23) collapse to familiar Navier-Stokes equations.

#### 2.4. Governing Equations for Non-Newtonian Fluid Flow in Curvilinear Coordinates

In curvilinear coordinates the Equations (2.22) and (2.23) become:

$$\begin{aligned}
& \mathcal{A}^{\frac{n-1}{2}} \frac{1}{J^2} (\alpha \Omega_{\eta\eta} - 2\beta \Omega_{\eta\xi} + \gamma \Omega_{\xi\xi}) \\
& + \frac{(n-1)}{2J^2} \mathcal{A}^{\frac{n-3}{2}} \left[ (\mathcal{A}_\eta x_\xi - \mathcal{A}_\xi x_\eta) (\Omega_\eta x_\xi - \Omega_\xi x_\eta) + (\mathcal{A}_\xi y_\eta - \mathcal{A}_\eta y_\xi) (\Omega_\xi y_\eta - \Omega_\eta y_\xi) \right] \\
& - \frac{(n-1)(n-3)}{2J} \mathcal{A}^{\frac{n-5}{2}} \left[ \mathcal{B} (\mathcal{A}_\eta x_\xi - \mathcal{A}_\xi x_\eta) - \mathcal{C} (\mathcal{A}_\xi y_\eta - \mathcal{A}_\eta y_\xi) \right] \\
& - \frac{(n-1)}{J} \mathcal{A}^{\frac{n-3}{2}} \left[ (\mathcal{B}_\eta x_\xi - \mathcal{B}_\xi x_\eta) - (\mathcal{C}_\xi y_\eta - \mathcal{C}_\eta y_\xi) \right] \\
& = Re \left\{ \Omega_t + \frac{1}{J} \left[ (u y_\eta \Omega_\xi - u y_\xi \Omega_\eta) + (v x_\xi \Omega_\eta - v x_\eta \Omega_\xi) \right] \right\}
\end{aligned} \tag{2.28}$$

$$\alpha \psi_{\eta\eta} - 2\beta \psi_{\eta\xi} + \gamma \psi_{\xi\xi} = -J^2 \Omega \tag{2.29}$$

where subscripts denote partial differentiation and  $\alpha$ ,  $\beta$  and  $\gamma$  are the coordinate transformation metrics and  $J$  is the Jacobian of the coordinate transformation accordingly which will be defined explicitly in the next chapter. Then  $\mathcal{A}$ ,  $\mathcal{B}$  and  $\mathcal{C}$  can be given explicitly,

$$\mathcal{A} = 2 \left[ \frac{y_\eta}{J} u_\xi - \frac{y_\xi}{J} u_\eta \right]^2 + 2 \left[ \frac{x_\xi}{J} v_\eta - \frac{x_\eta}{J} v_\xi \right]^2 + 2 \left[ \left( \frac{x_\xi}{J} u_\eta - \frac{x_\eta}{J} u_\xi \right) + \left( \frac{y_\eta}{J} v_\xi - \frac{y_\xi}{J} v_\eta \right) \right]^2 \tag{2.30}$$

$$\mathcal{B} = \left( \frac{y_\eta}{J} \mathcal{A}_\xi - \frac{y_\xi}{J} \mathcal{A}_\eta \right) \left( \frac{y_\eta}{J} u_\xi - \frac{y_\xi}{J} u_\eta \right) + \frac{1}{2J^2} \left[ (x_\xi \mathcal{A}_\eta - x_\eta \mathcal{A}_\xi) (x_\xi u_\eta - x_\eta u_\xi + y_\eta v_\xi - y_\xi v_\eta) \right] \quad (2.31)$$

$$\mathcal{C} = \left( \frac{x_\xi}{J} \mathcal{A}_\eta - \frac{x_\eta}{J} \mathcal{A}_\xi \right) \left( \frac{x_\xi}{J} v_\eta - \frac{x_\eta}{J} v_\xi \right) + \frac{1}{2J^2} \left[ (y_\eta \mathcal{A}_\xi - y_\xi \mathcal{A}_\eta) (x_\xi u_\eta - x_\eta u_\xi + y_\eta v_\xi - y_\xi v_\eta) \right] \quad (2.32)$$

where  $\mathcal{A}$  is the curvilinear representation of the second invariant of the rate of strain tensor  $I_2$ ,  $\mathcal{B}$  is the curvilinear form of expression  $G_1$  and  $\mathcal{C}$  is the curvilinear form of expression  $G_2$  that have been given explicitly in Equations (2.24), (2.25) and (2.26) respectively for the rectangular coordinates. (See Appendix A for detailed curvilinear transformation expressions of the derivatives of  $u$  and  $v$  with respect to  $x$  and  $y$ )

### 3. NUMERICAL METHOD

#### 3.1. Grid Generation

Numerical grid generation arose from the need to compute solutions to partial differential equations of fluid dynamics on physical regions with complex geometry. By transforming the physical region into a simpler region, one removes the complication of the shape of the physical region from the problem. Such transformations can be viewed as a general curvilinear coordinate system for the physical region. The classical techniques of transforming problems to polar, cylindrical, or spherical coordinates are special cases. A cost of using such coordinate systems is an increase in complexity of the transformed equations, i.e., those equations modeling the problem to be solved. An advantage of this technique is that the boundary conditions become easier to approximate accurately.

In many applications, it is possible to transform the physical domain to a square in two dimensions in such a manner that the boundary of the square corresponds to the boundary of the physical domain (see Figure 3.1). The square is called the computational domain and the transformation gives rise to a body fitted coordinate system. The coordinate lines in this coordinate system are given by the images of uniform coordinate lines in the computational domain. In such coordinate systems, it is relatively easy to make accurate implementations of numerical boundary conditions.

In this development, the Jacobian of the transformation is required to be nonzero, and consequently the transformation has an inverse. Because the grids are first chosen in computational domain and then mapped to physical domain, it is natural to view the transformation as a mapping from computational to physical domain (see Figure 3.1 [18]). In addition, if a set of points is chosen in computational domain, then the inverse transformation carries these points to points in physical domain, where they form a *grid* (see Figure 3.2 [18]).

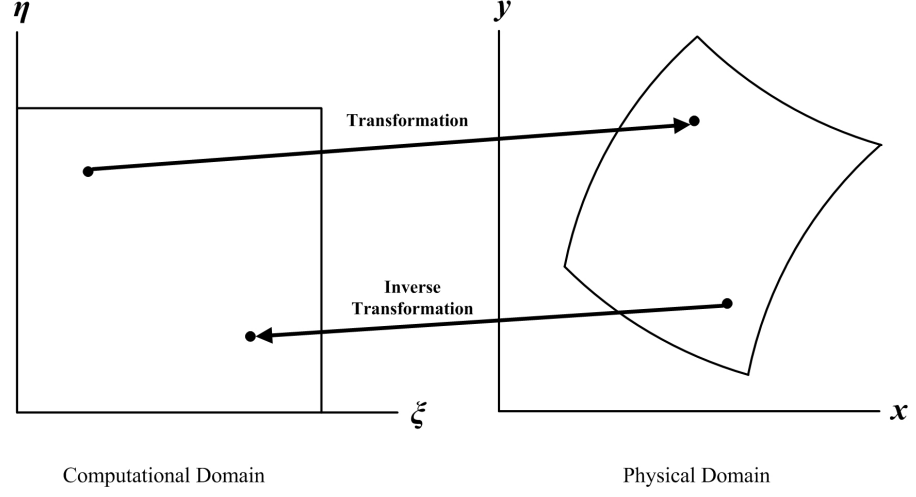


Figure 3.1. Transformation, map, or coordinate system

### 3.1.1. Grid Generation Equations

Consider a dependent variable in the governing flow equations, such as the  $x$ -component of velocity  $u$ . Let  $u = u(x, y)$ , where  $x = x(\xi, \eta)$  and  $y = y(\xi, \eta)$ . The total differential of  $u$  is given by;

$$du = \frac{\partial u}{\partial x} dx + \frac{\partial u}{\partial y} dy \quad (3.1)$$

It follows that

$$\frac{\partial u}{\partial \xi} = \frac{\partial u}{\partial x} \frac{\partial x}{\partial \xi} + \frac{\partial u}{\partial y} \frac{\partial y}{\partial \xi} \quad (3.2)$$

and

$$\frac{\partial u}{\partial \eta} = \frac{\partial u}{\partial x} \frac{\partial x}{\partial \eta} + \frac{\partial u}{\partial y} \frac{\partial y}{\partial \eta} \quad (3.3)$$

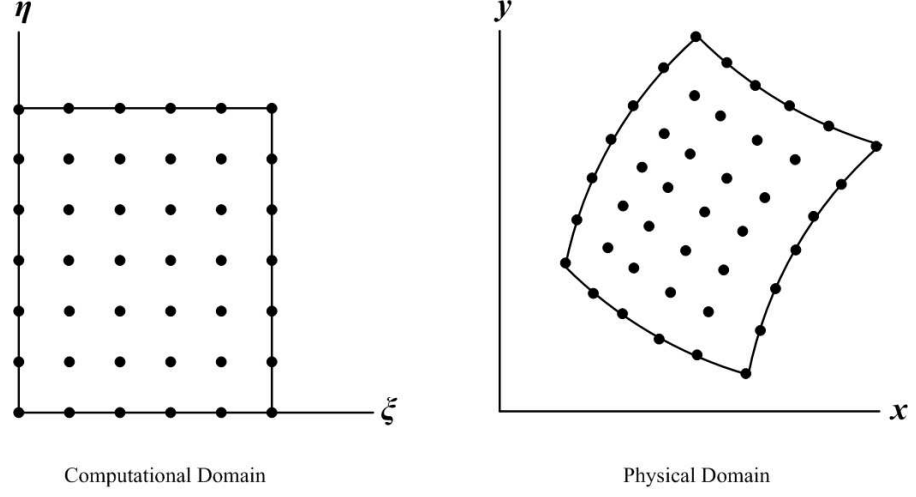


Figure 3.2. A grid

Equations (3.2) and (3.3) can be viewed as two equations for the two unknowns  $\frac{\partial u}{\partial x}$  and  $\frac{\partial u}{\partial y}$ , Solving the system of Equations (3.2) and (3.3) for  $\frac{\partial u}{\partial x}$  using Cramer's rule, we have

$$\frac{\partial u}{\partial x} = \frac{\begin{vmatrix} \frac{\partial u}{\partial \xi} & \frac{\partial y}{\partial \xi} \\ \frac{\partial u}{\partial \eta} & \frac{\partial y}{\partial \eta} \end{vmatrix}}{\begin{vmatrix} \frac{\partial x}{\partial \xi} & \frac{\partial y}{\partial \xi} \\ \frac{\partial x}{\partial \eta} & \frac{\partial y}{\partial \eta} \end{vmatrix}} \quad (3.4)$$

In Equation (3.4), the denominator determinant is identified as the *Jacobian determinant*, denoted by;

$$J \equiv \frac{\partial(x, y)}{\partial(\xi, \eta)} \equiv \begin{vmatrix} \frac{\partial x}{\partial \xi} & \frac{\partial y}{\partial \xi} \\ \frac{\partial x}{\partial \eta} & \frac{\partial y}{\partial \eta} \end{vmatrix} \quad (3.5)$$

Hence Equation (3.4) can be re-written as

$$\frac{\partial u}{\partial x} = \frac{1}{J} \left[ \frac{\partial u}{\partial \xi} \frac{\partial y}{\partial \eta} - \frac{\partial u}{\partial \eta} \frac{\partial y}{\partial \xi} \right] \quad (3.6)$$

Now let us return to Equations (3.2) and (3.3), and solve for  $\frac{\partial u}{\partial y}$ .

$$\frac{\partial u}{\partial y} = \frac{\begin{vmatrix} \frac{\partial x}{\partial \xi} & \frac{\partial u}{\partial \xi} \\ \frac{\partial x}{\partial \eta} & \frac{\partial u}{\partial \eta} \end{vmatrix}}{\begin{vmatrix} \frac{\partial x}{\partial \xi} & \frac{\partial y}{\partial \xi} \\ \frac{\partial x}{\partial \eta} & \frac{\partial y}{\partial \eta} \end{vmatrix}} \quad (3.7)$$

or,

$$\frac{\partial u}{\partial y} = \frac{1}{J} \left[ \frac{\partial u}{\partial \eta} \frac{\partial x}{\partial \xi} - \frac{\partial u}{\partial \xi} \frac{\partial x}{\partial \eta} \right] \quad (3.8)$$

If we apply the chain rule we obtain,

$$\frac{\partial u}{\partial x} = \frac{\partial u}{\partial \xi} \frac{\partial \xi}{\partial x} + \frac{\partial u}{\partial \eta} \frac{\partial \eta}{\partial x} \quad (3.9)$$

$$\frac{\partial u}{\partial y} = \frac{\partial u}{\partial \xi} \frac{\partial \xi}{\partial y} + \frac{\partial u}{\partial \eta} \frac{\partial \eta}{\partial y} \quad (3.10)$$

thus  $\xi_x$ ,  $\xi_y$ ,  $\eta_x$  and  $\eta_y$  are the metrics of transformation and can be defined as,

$$\xi_x = \frac{1}{J} \frac{\partial y}{\partial \eta} \quad (3.11)$$

$$\xi_y = -\frac{1}{J} \frac{\partial x}{\partial \eta} \quad (3.12)$$

$$\eta_x = -\frac{1}{J} \frac{\partial y}{\partial \xi} \quad (3.13)$$

$$\eta_y = \frac{1}{J} \frac{\partial x}{\partial \xi} \quad (3.14)$$

where  $J$  is the *Jacobian* of the coordinate transformation,  $\xi$  and  $\eta$  are the transformed coordinates.

As can be seen from Figure 3.1 we need an analytic relation between the two coordinate systems : computational domain  $(\xi, \eta)$  and physical domain  $(x, y)$ . After that brief introduction to coordinate transformation, we consider the second derivatives of  $u$  with respect to  $\xi$ ,  $\eta$  and mixed derivative,

$$u_{\xi\xi} = u_x x_{\xi\xi} + u_y y_{\xi\xi} + u_{xx} x_\xi^2 + u_{yy} y_\xi^2 + 2u_{xy} x_\xi y_\xi \quad (3.15)$$

$$u_{\eta\eta} = u_x x_{\eta\eta} + u_y y_{\eta\eta} + u_{xx} x_\eta^2 + u_{yy} y_\eta^2 + 2u_{xy} x_\eta y_\eta \quad (3.16)$$

$$u_{\xi\eta} = u_x x_{\xi\eta} + u_y y_{\xi\eta} + u_{xx} x_\xi x_\eta + u_{yy} y_\xi y_\eta + u_{xy} (x_\eta y_\xi + x_\xi y_\eta) \quad (3.17)$$

Then we have a system of Equations (3.15), (3.16) and (3.17). If we re-write this system in matrix form as  $b = Ax$  we will get:

$$\begin{bmatrix} u_{\xi\xi} - u_x x_{\xi\xi} - u_y y_{\xi\xi} \\ u_{\eta\eta} - u_x x_{\eta\eta} - u_y y_{\eta\eta} \\ u_{\xi\eta} - u_x x_{\xi\eta} - u_y y_{\xi\eta} \end{bmatrix} = \begin{bmatrix} x_\xi^2 & y_\xi^2 & 2x_\xi y_\xi^2 \\ x_\eta^2 & y_\eta^2 & 2x_\eta y_\eta^2 \\ x_\xi x_\eta & y_\xi y_\eta & y_\xi x_\eta + y_\eta x_\xi \end{bmatrix} \begin{bmatrix} u_{xx} \\ u_{yy} \\ u_{xy} \end{bmatrix} \quad (3.18)$$

If we apply the Cramer's Rule to this system, the unknown definitions  $u_{xx}$ ,  $u_{yy}$  and  $u_{xy}$  can be found as;

$$\begin{aligned}
u_{xx} = & \left(\frac{y_\eta}{J}\right)^2 u_{\xi\xi} + \left(\frac{y_\xi}{J}\right)^2 u_{\eta\eta} - 2\frac{y_\eta y_\xi}{J^2} u_{\xi\eta} \\
& + \frac{1}{J^3} \left[ y_\xi (y_\eta^2 x_{\xi\xi} + y_\xi^2 x_{\eta\eta} - 2y_\eta y_\xi x_{\xi\eta}) - x_\xi (y_\eta^2 y_{\xi\xi} + y_\xi^2 y_{\eta\eta} - 2y_\eta y_\xi y_{\xi\eta}) \right] u_\eta \\
& + \frac{1}{J^3} \left[ x_\eta (y_\eta^2 y_{\xi\xi} + y_\xi^2 y_{\eta\eta} - 2y_\eta y_\xi y_{\xi\eta}) - y_\eta (y_\eta^2 x_{\xi\xi} + y_\xi^2 x_{\eta\eta} - 2y_\eta y_\xi x_{\xi\eta}) \right] u_\xi
\end{aligned} \quad (3.19)$$

$$\begin{aligned}
u_{yy} = & \left(\frac{x_\eta}{J}\right)^2 u_{\xi\xi} + \left(\frac{x_\xi}{J}\right)^2 u_{\eta\eta} - 2\frac{x_\eta x_\xi}{J^2} u_{\xi\eta} \\
& + \frac{1}{J^3} \left[ y_\xi (x_\eta^2 x_{\xi\xi} + x_\xi^2 x_{\eta\eta} - 2x_\xi x_\eta x_{\xi\eta}) - x_\xi (x_\eta^2 y_{\xi\xi} + x_\xi^2 y_{\eta\eta} - 2x_\eta x_\xi y_{\xi\eta}) \right] u_\eta \\
& + \frac{1}{J^3} \left[ x_\eta (x_\eta^2 y_{\xi\xi} + x_\xi^2 y_{\eta\eta} - 2x_\eta x_\xi y_{\xi\eta}) - y_\eta (x_\eta^2 x_{\xi\xi} + x_\xi^2 x_{\eta\eta} - 2x_\xi x_\eta x_{\xi\eta}) \right] u_\xi
\end{aligned} \quad (3.20)$$

and

$$\begin{aligned}
u_{xy} = & -\frac{x_\eta y_\eta}{J^2} u_{\xi\xi} - \frac{x_\xi y_\xi}{J^2} u_{\eta\eta} + \frac{x_\xi y_\eta + x_\eta y_\xi}{J^2} u_{\xi\eta} \\
& + \frac{1}{J^3} \left[ x_\xi (x_\eta y_\eta y_{\xi\xi} + x_\xi y_\xi y_{\eta\eta} - (x_\xi y_\eta + x_\eta y_\xi) y_{\xi\eta}) \right. \\
& \quad \left. - y_\xi (x_\eta y_\eta x_{\xi\xi} + x_\xi y_\xi x_{\eta\eta} - (x_\xi y_\eta + x_\eta y_\xi) x_{\xi\eta}) \right] u_\eta \\
& + \frac{1}{J^3} \left[ y_\eta (x_\eta y_\eta x_{\xi\xi} + x_\xi y_\xi x_{\eta\eta} - (x_\xi y_\eta + x_\eta y_\xi) x_{\xi\eta}) \right. \\
& \quad \left. - x_\eta (x_\eta y_\eta y_{\xi\xi} + x_\xi y_\xi y_{\eta\eta} - (x_\xi y_\eta + x_\eta y_\xi) y_{\xi\eta}) \right] u_\xi
\end{aligned} \quad (3.21)$$

where  $J$  denotes the *Jacobian* of the coordinate transformation as described in Equation (3.5) and subscripts denote the partial derivatives.



The coordinate transformation should have an inverse so it has to be unique. If we consider the second derivative of  $u$  with respect to  $x$ ,  $y$  and mixed derivative, we can write,

$$u_{xx} = u_{\xi\xi}\xi_x^2 + u_{\eta\eta}\eta_x^2 + u_{\xi\eta}\xi_x\eta_x + u_{\eta\xi}\eta_x\xi_x + u_{\xi\xi\xi_x} \quad (3.22)$$

$$u_{yy} = u_{\xi\xi}\xi_y^2 + u_{\eta\eta}\eta_y^2 + u_{\xi\eta}\xi_y\eta_y + u_{\eta\xi}\eta_y\xi_y + u_{\xi\xi\xi_y} \quad (3.23)$$

$$u_{xy} = u_{\xi\xi}\xi_x\xi_y + u_{\eta\eta}\eta_x\eta_y + u_{\xi\eta}(\eta_x\xi_y + \xi_x\eta_y) + u_{\eta\xi}\eta_x\xi_y + u_{\xi\xi\xi_y} \quad (3.24)$$

The second derivative representations of  $u$  i.e  $u_{xx}$ ,  $u_{yy}$  and  $u_{xy}$  must be identical no matter how we describe them. So from previous equations we derived one can easily show that Equation (3.19) is identical to Equation (3.22) and Equation (3.20) is identical to Equation (3.23). In Equation (3.19) the coefficient of  $u_{\eta}$  must be equal to the coefficient of  $u_{\eta}$  in Equation (3.22) and then

$$\eta_{xx} = \frac{1}{J^3} \left[ y_{\xi} (y_{\eta}^2 x_{\xi\xi} + y_{\xi}^2 x_{\eta\eta} - 2y_{\eta} y_{\xi} x_{\xi\eta}) - x_{\xi} (y_{\eta}^2 y_{\xi\xi} + y_{\xi}^2 y_{\eta\eta} - 2y_{\xi} y_{\eta} y_{\xi\eta}) \right] \quad (3.25)$$

$$\xi_{xx} = \frac{1}{J^3} \left[ x_{\eta} (y_{\eta}^2 y_{\xi\xi} + y_{\xi}^2 y_{\eta\eta} - 2y_{\xi} y_{\eta} y_{\xi\eta}) - y_{\eta} (y_{\eta}^2 x_{\xi\xi} + y_{\xi}^2 x_{\eta\eta} - 2y_{\eta} y_{\xi} x_{\xi\eta}) \right] \quad (3.26)$$

in the same manner,

$$\eta_{yy} = \frac{1}{J^3} \left[ y_{\xi} (x_{\eta}^2 x_{\xi\xi} + x_{\xi}^2 x_{\eta\eta} - 2x_{\xi} x_{\eta} x_{\xi\eta}) - x_{\xi} (x_{\eta}^2 y_{\xi\xi} + x_{\xi}^2 y_{\eta\eta} - 2x_{\eta} x_{\xi} y_{\xi\eta}) \right] \quad (3.27)$$

$$\xi_{yy} = \frac{1}{J^3} \left[ x_{\eta} (x_{\eta}^2 y_{\xi\xi} + x_{\xi}^2 y_{\eta\eta} - 2x_{\eta} x_{\xi} y_{\xi\eta}) - y_{\eta} (x_{\eta}^2 x_{\xi\xi} + x_{\xi}^2 x_{\eta\eta} - 2x_{\xi} x_{\eta} x_{\xi\eta}) \right] \quad (3.28)$$

The most common partial differential equation used for elliptic grid generation is the Poisson equation:

$$\nabla^2 \xi = \xi_{xx} + \xi_{yy} = P(\xi, \eta) \quad (3.29)$$

$$\nabla^2 \eta = \eta_{xx} + \eta_{yy} = Q(\xi, \eta) \quad (3.30)$$

and with boundary conditions specified by

$$\begin{aligned} \xi &= F(x, y), \\ \eta &= G(x, y), \end{aligned} \quad (3.31)$$

where  $(\xi, \eta)$  and  $(x, y)$  are the curvilinear and cartesian coordinate frames respectively. If we put Equations (3.26) and (3.28) into Equation (3.29) we will get;

$$(x_\eta^2 + y_\eta^2)x_{\xi\xi} - 2(x_\xi x_\eta + y_\xi y_\eta)x_{\xi\eta} + (x_\xi^2 + y_\xi^2)x_{\eta\eta} = -J^2(Px_\xi + Qx_\eta) \quad (3.32)$$

and if we put Equations (3.25) and (3.27) into Equation (3.30) we will get,

$$(x_\eta^2 + y_\eta^2)y_{\xi\xi} - 2(x_\xi x_\eta + y_\xi y_\eta)y_{\xi\eta} + (x_\xi^2 + y_\xi^2)y_{\eta\eta} = -J^2(Py_\xi + Qy_\eta) \quad (3.33)$$

then as a generic representation we can obtain the classical elliptic grid generation equations as:

$$\alpha x_{\xi\xi} - \beta x_{\xi\eta} + \gamma x_{\eta\eta} = -J^2(Px_\xi + Qx_\eta) \quad (3.34)$$

$$\alpha y_{\xi\xi} - \beta y_{\xi\eta} + \gamma y_{\eta\eta} = -J^2(Py_\xi + Qy_\eta) \quad (3.35)$$

where;

$$P = \frac{1}{J^3} \left[ x_\eta (\alpha y_{\xi\xi} - \beta y_{\xi\eta} + \gamma y_{\eta\eta}) - y_\eta (\alpha x_{\xi\xi} - \beta x_{\xi\eta} + \gamma x_{\eta\eta}) \right] \quad (3.36)$$

$$Q = \frac{1}{J^3} \left[ y_\xi (\alpha x_{\xi\xi} - \beta x_{\xi\eta} + \gamma x_{\eta\eta}) - x_\xi (\alpha y_{\xi\xi} - \beta y_{\xi\eta} + \gamma y_{\eta\eta}) \right] \quad (3.37)$$

$$\alpha = x_\eta^2 + y_\eta^2 \quad (3.38)$$

$$\beta = x_\xi x_\eta + y_\xi y_\eta \quad (3.39)$$

$$\gamma = x_\xi^2 + y_\xi^2 \quad (3.40)$$

The functions  $P$  and  $Q$  can be selected according to a specific need. The requirement may be clustering of grid points at some prescribed location (as in shock wave problems) or forcing orthogonality at the surface (as in heat transfer problems with temperature gradient at the surface). In this study these source terms  $P$  and  $Q$  are used for grid orthogonality at the surface to increase the accuracy of the numerical scheme.

### 3.1.2. Grid Generation for Cavity Problems

In this study we have adopted three different cavity geometries. These geometries are square geometry, polar geometry and arc-shaped geometry.

The grid inside the flow field in the square and polar cavities have been generated by elliptic grid generation technique.

The physical model of the square cavity is a unit square as in Figure 1.3. Only the top wall is moving with a constant velocity  $u_\infty$  and other the walls are stationary.

The physical model of the polar cavity can be seen in Figure 3.3. Only the bottom wall is moving with a constant rotational velocity  $u_\infty$  and other walls are stationary. This geometry is first described by Fuchs *et.al* [23] as an experimental setting. The details of the geometry can be found in Fuchs study [23]. The Reynolds number,  $Re$ , is based on the lid velocity which drives the fluid, the radius of the inner circle (i.e. the moving lid parameter) and the kinematic viscosity of the fluid as it has been described in detail in the previous chapter.

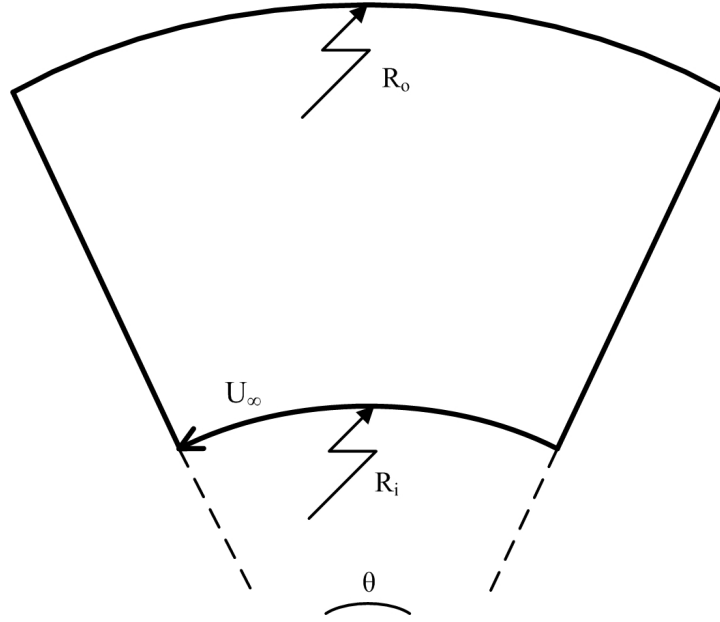


Figure 3.3. Physical model of polar cavity with a moving lid

The grid for the flow field in an arc-shaped cavity has been generated by elliptic grid generation technique.

The physical model of arc-shaped cavity problem is shown in Figure 3.4. This geometry is inspired by the work of Chang *et.al.* [12]. The enclosure of width  $L$  is confined by an arc-shape wall and a flat lid which is moving at a velocity of  $u_\infty$ . The arc shape is defined by the expression  $(x-p)^2 + (y-q)^2 = R^2$  which denotes a circle of radius  $R$  with the center located at  $(p, q)$ . In this study, the ratios  $p/L, q/L$ , and  $R/L$  were fixed at  $1/2, 1/2\sqrt{3}$  and  $1/\sqrt{3}$ , respectively [12].

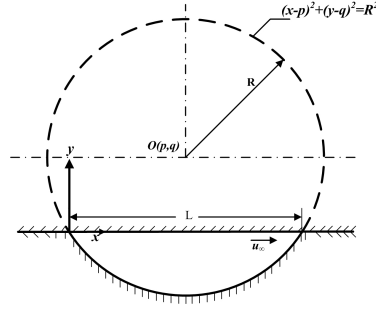
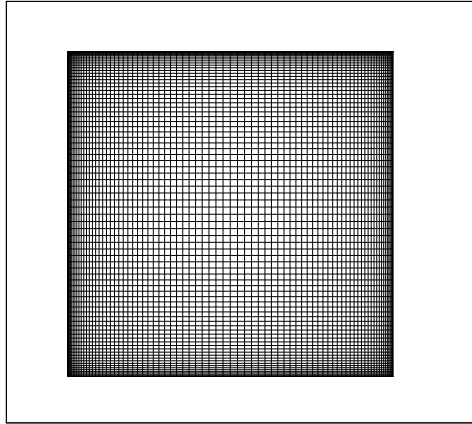


Figure 3.4. Physical model of arc-shape cavity with a moving lid

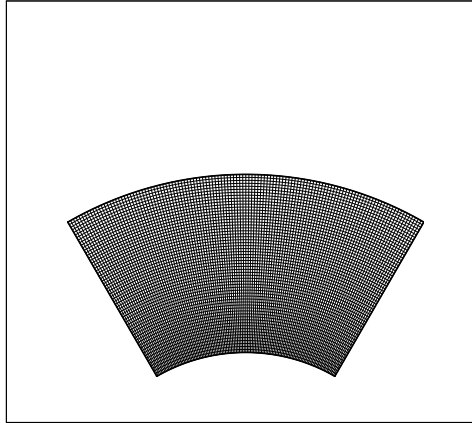
Examples of grids generated for square, polar and arc cavities by body-fitted coordinate transformation (i.e. elliptic grid generation) are demonstrated in Figures 3.5(a), 3.5(b), 3.5(c), respectively.

### 3.2. Discretization of Partial Differential Equations

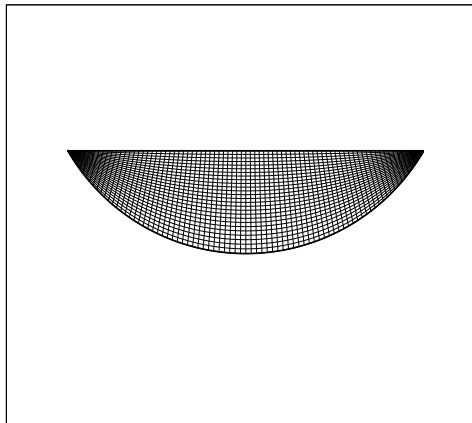
Analytical solutions for partial differential equations (PDEs) involve closed-form expressions which give the variation of the dependent variables *continuously* throughout the domain. In contrast, numerical solutions can give answers only at discrete points in the domain, called *grid points*. The differentials of the dependent variables appearing in partial differential equations must be expressed as approximate expressions in order to solve the governing flow equations by using a numerical technique.



(a) Elliptic grid generated for the square geometry with a clustering parameter= 1.8



(b) Elliptic grid generated for the polar geometry



(c) Elliptic grid generated for the arc-shaped geometry

Figure 3.5. Sample grids

In this study the *method of finite-differences* has been used. The philosophy of finite difference method is to replace the partial derivatives appearing in the governing equation of fluid dynamics (as derived in the previous chapter) with algebraic difference quotients, yielding a system of *algebraic equations* which can be solved for the flow field variables at the specific, discrete grid points in the flow.

In order to demonstrate the discretization of the equations by finite difference scheme we will discretize the aforementioned Newtonian flow equations. We used forward difference scheme in time and centered difference scheme in space. Recalling the Equation (2.13), vorticity-transport equation in conservative form, the discretized form is,

$$\begin{aligned}
& \frac{\Omega_{i,j}^{n+1} - \Omega_{i,j}^{n-1}}{\Delta t} + \frac{1}{J} \left[ \left( \frac{y_{i,j+1} - y_{i,j-1}}{2\Delta\eta} \right) \left( \frac{\Omega_{i+1,j}^n u_{i+1,j}^n - \Omega_{i-1,j}^n u_{i-1,j}^n}{2\Delta\xi} \right) \right. \\
& - \left( \frac{y_{i+1,j} - y_{i-1,j}}{2\Delta\xi} \right) \left( \frac{\Omega_{i,j+1}^n u_{i,j+1}^n - \Omega_{i,j-1}^n u_{i,j-1}^n}{2\Delta\eta} \right) \\
& + \left( \frac{x_{i+1,j} - x_{i-1,j}}{2\Delta\xi} \right) \left( \frac{\Omega_{i,j+1}^n v_{i+1,j}^n - \Omega_{i,j-1}^n v_{i,j-1}^n}{2\Delta\eta} \right) \\
& \left. - \left( \frac{x_{i,j+1} - x_{i,j-1}}{2\Delta\eta} \right) \left( \frac{\Omega_{i+1,j}^n v_{i+1,j}^n - \Omega_{i-1,j}^n v_{i-1,j}^n}{2\Delta\xi} \right) \right] \\
& = \frac{1}{ReJ^2} \left[ \alpha_{i,j} \left( \frac{\Omega_{i+1,j}^n - 2\Omega_{i,j}^n + \Omega_{i-1,j}^n}{\Delta\xi^2} \right) \right. \\
& - 2\beta_{i,j} \left( \frac{\Omega_{i+1,j+1}^n - \Omega_{i+1,j-1}^n - \Omega_{i-1,j+1}^n + \Omega_{i-1,j-1}^n}{4\Delta\xi\Delta\eta} \right) \\
& \left. + \gamma_{i,j} \left( \frac{\Omega_{i,j+1}^n - 2\Omega_{i,j}^n + \Omega_{i,j-1}^n}{\Delta\eta^2} \right) \right] \quad (3.41)
\end{aligned}$$

where  $\Delta t$  is the time step,  $\Delta\xi$  and  $\Delta\eta$  are the grid sizes which are fixed to unity.  $n$  denotes the time level where  $+1$  and  $-1$  refer to the adjacent time levels. The discretized stream function equation is

$$\begin{aligned}
& \alpha_{i,j} \left( \frac{\psi_{i+1,j}^n - 2\psi_{i,j}^n + \psi_{i-1,j}^n}{\Delta\xi^2} \right) - 2\beta_{i,j} \left( \frac{\psi_{i+1,j+1}^n - \psi_{i+1,j-1}^n - \psi_{i-1,j+1}^n + \psi_{i-1,j-1}^n}{4\Delta\xi\Delta\eta} \right) \\
& + \gamma_{i,j} \left( \frac{\psi_{i,j+1}^n - 2\psi_{i,j}^n + \psi_{i,j-1}^n}{\Delta\eta^2} \right) = -J^2\Omega_{i,j} \quad (3.42)
\end{aligned}$$

where  $\alpha$ ,  $\beta$  and  $\gamma$  denote the coordinate transformation metrics and  $J$  is the *Jacobian* of the transformation.

After the coordinate transformation functions  $\xi = \xi(x, y)$  and  $\eta = \eta(x, y)$  denoting the curvilinear coordinate system are obtained numerically, governing equations are discretized into a set of simultaneous algebraic equations (as in Equations (3.41), (3.42)) and then the resultant algebraic equations are solved for each discrete node surrounding the grid points.

The finite difference equations obtained for  $\psi$  and  $\Omega$  may be solved individually. The 3<sup>rd</sup> order Adams Bashforth method is well accepted and hence is adopted in this study to deal with the highly non-linear unsteady vorticity transport Equation (2.28), on the other hand the Successive Over Relaxation (SOR) method with Chebyshev acceleration is used to solve Equation (2.29) for stream function,  $\psi$ .

### 3.2.1. Time Integration Algorithm

We have got two coupled partial differential equations (PDEs) to be solved. The first PDE is the unsteady vorticity transport equation in curvilinear coordinates in which the stress term has been described with a power law constitutive model (2.17). In order to solve this equation we have discretized all terms with finite difference scheme in the same manner as (3.41) and (3.42). The resultant algebraic expression is to be solved explicitly because of the highly non-linear and unsteady nature. To manage this unsteadiness and nonlinearity we have adopted an accurate explicit scheme, *Adams-Bashforth*.

For demonstration purposes, we consider the following system,

$$\frac{du}{dt} = f(u, t) \quad (3.43)$$



Adams Bashforth Methods are a class of explicit methods including the simple forward Euler (Forward Time Centered Space so called FTCS) method for which the discretized system is:

$$u^{n+1} = u^n + \Delta t f^n \quad (3.44)$$

applying the popular second-order Adams Bashforth method, the discretized system can be written as,

$$u^{n+1} = u^n + \frac{\Delta t}{2} [3f^n - f^{n-1}] \quad (3.45)$$

the still more accurate third-order method gives,

$$u^{n+1} = u^n + \frac{\Delta t}{12} [23f^n - 16f^{n-1} + 5f^{n-2}] \quad (3.46)$$

and even higher-order versions can be considered, see Table (3.1).

Table 3.1. Explicit Adams-Bashforth Methods

p	Adams Bashforth Methods	Local Error (for $\zeta_n \in [x_{n-p}, x_{n+1}]$ )
0	$u^{n+1} = u^n + \Delta t f^n$	$\frac{\Delta t^2}{2} u''(\zeta^n)$
1	$u^{n+1} = u^n + \frac{\Delta t}{2} [3f^n - f^{n-1}]$	$\frac{5\Delta t^3}{12} u^{(3)}(\zeta^n)$
2	$u^{n+1} = u^n + \frac{\Delta t}{12} [23f^n - 16f^{n-1} + 5f^{n-2}]$	$\frac{3\Delta t^4}{8} u^{(4)}(\zeta^n)$
3	$u^{n+1} = u^n + \frac{\Delta t}{24} [55f^n - 59f^{n-1} + 37f^{n-2} - 9f^{n-3}]$	$\frac{251\Delta t^5}{720} u^{(5)}(\zeta^n)$

### 3.2.2. Space Integration Algorithm

The second partial differential equation is stream function Equation(2.14) in curvilinear coordinates which can be classified as an elliptic equation. Any numerical scheme introduced to solve an elliptic equation can be used to solve this Poisson equation. If an elliptic PDE discretized by the use of finite difference method, a linear system of equation is obtained as

$$A\mathbf{x} = \mathbf{b} \quad (3.47)$$

where  $A$  is the matrix of coefficients,  $\mathbf{x}$  is the column vector of variables, and  $\mathbf{b}$  is the input column vector. The Successive Over Relaxation method (SOR) is a method of solving a linear system of equations like Equation (3.47). The following description is based on the book by H. William [25]. This method can be written for each component in one space dimension and in condensed form as:

$$x_i^{(k)} = \omega \bar{x}_i^{(k)} + (1 - \omega) \bar{x}_i^{(k-1)} \quad (3.48)$$

where  $\bar{x}$  denotes an iterate which is an initial guess and/or result from previous iteration and  $\omega$  is the extrapolation factor and where  $i$  refer to the node and  $k$  is for the iteration level. The idea is to choose a value for  $\omega$  that will accelerate the rate of convergence of the iterates to the solution.

In matrix terms, the SOR algorithm can be re-written as

$$\mathbf{x}^{(k)} = \mathbf{x}^{(k-1)} - (L + D)^{-1} \cdot [(L + D + U)\mathbf{x}^{k-1} - \mathbf{b}] \quad (3.49)$$

where the matrices  $D$ ,  $L$ , and  $U$  represent the diagonal, strictly lower-triangular, and strictly upper-triangular parts of  $A$ , respectively. The term in square brackets is just the residual vector  $\mathcal{R}^{k-1}$ , so Equation (3.49) becomes

$$\mathbf{x}^{(k)} = \mathbf{x}^{(k-1)} - (L + D)^{-1} \cdot \mathcal{R}^{k-1} \quad (3.50)$$

if we *overcorrect* the Equation (3.50), the resultant equation will be

$$\mathbf{x}^{(k)} = \mathbf{x}^{(k-1)} - \omega (L + D)^{-1} \cdot \mathcal{R}^{k-1} \quad (3.51)$$

Here  $\omega$  is called *overrelaxation parameter*, and the method is called *successive overrelaxation* (SOR). This method is convergent only for  $0 < \omega < 2$  and the optimal choice for  $\omega$  is given by

$$\omega = \frac{2}{1 + \sqrt{1 - \rho_{jacob}^2}} \quad (3.52)$$

where as a reference definition the value of  $\rho_{jacob}$  can be given for a model problem on a rectangular  $J \times L$  grid allowing for the possibility that the grid sizes  $\Delta x \neq \Delta y$ :

$$\rho_{jacob} = \frac{\cos \frac{\pi}{J} + \left( \frac{\Delta x}{\Delta y} \right)^2 \cos \frac{\pi}{L}}{1 + \left( \frac{\Delta x}{\Delta y} \right)^2} \quad (3.53)$$

For this choice, the spectral radius for SOR is

$$\rho_{SOR} = \left( \frac{\rho_{jacob}}{1 + \sqrt{1 - \rho_{jacob}^2}} \right)^2 \quad (3.54)$$

Choosing  $\omega$  for a problem for which the answer is not known analytically is the weak point of SOR. One way to choose  $\omega$  is to map the problem approximately onto a known problem, replacing the coefficients of the equation by average values. However the known problem must have the same grid size and boundary conditions as the actual problem.

In this study we have used Successive Over Relaxation Method with Chebyshev acceleration. In SOR with Chebyshev acceleration, we used odd-even ordering and changed  $\omega$  at each half sweep according to the following prescription:

$$\begin{aligned}
 \omega^{(0)} &= 1 \\
 \omega^{(1/2)} &= 1/(1 - \rho_{jacobi}^2/2) \\
 \omega^{(n+1/2)} &= 1/(1 - \rho_{jacobi}^2 \omega^{(n)}/4), \quad n = 1/2, 1, \dots, \infty \\
 \omega^{(\infty)} &\rightarrow \omega_{optimal}
 \end{aligned} \tag{3.55}$$

### 3.3. Code Validation

The numerical method described in the previous sections is tested by solving a number of Newtonian flow cases i.e.  $n = 1$  in Equation (2.28). Example flows presented herein are a lid-driven square cavity flow, a lid-driven polar cavity flow and a lid-driven arc-shaped cavity flow. For the validation of the code, the results are compared with the results by previous researchers and very good agreement with the results for these cases in literature [8], [4], [12], [23], [24], [26] has been obtained for several Reynolds numbers.

Lid driven square cavity flows at  $Re = 100$  and  $Re = 1000$  are considered below to confirm the accuracy of the present numerical method. For the solution of the unsteady Navier-Stokes equations in terms of stream function and vorticity Adams-Bashforth and SOR methods are used as explained in previous chapter. The computational domain is discretized by an unequally spaced  $81 \times 81$  grid with concentration of the grid near the wall region with a clustering parameter 1.1. The steady state results are obtained at dimensionless time  $t = 20$ . The calculated streamline contours are shown in Figure 3.6(a) and 3.6(c) for  $Re = 100$  and  $Re = 1000$  respectively.

For an assessment of the accuracy of the present results, the  $u$  velocity component through the vertical centerline of the cavity is compared with the corresponding numerical results of Ghia *et al.* [8] in Figure 3.7 for both  $Re = 100$  and  $Re = 1000$ . The comparison shows good agreement with the results in literature.

Table 3.2 tabulates the minimum streamline value and the center location of the primary vortex for  $Re = 100$  and  $Re = 1000$  along with similar result found in literature.

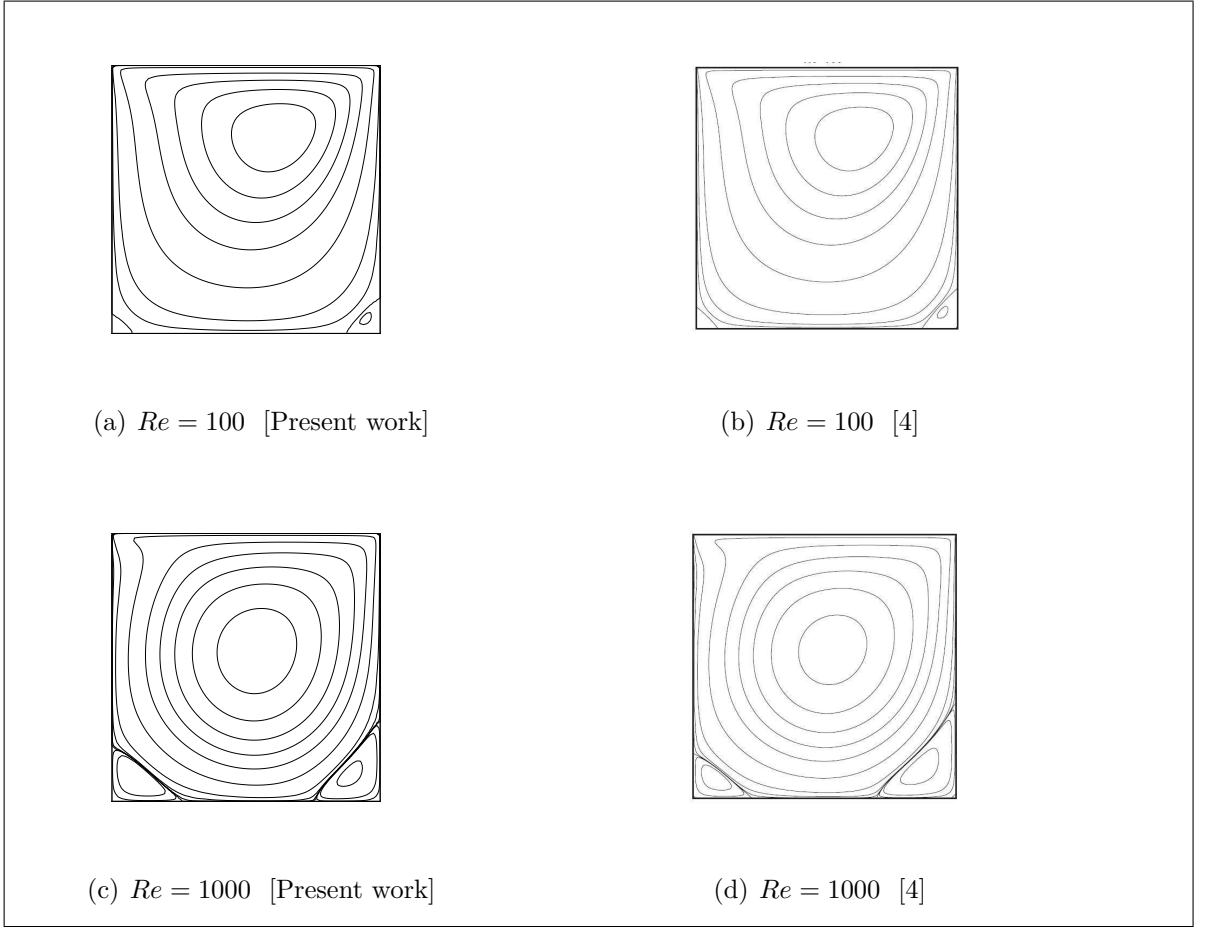


Figure 3.6. Comparison of Newtonian results of square cavity for  $Re = 100$  and  $Re = 1000$ . The streamline value equals 0 on the cavity boundary and contour levels shown for each plot are from the inner most contour  $-0.111$ ,  $-0.095$ ,  $-0.075$ ,  $-0.055$ ,  $-0.035$ ,  $-0.015$ ,  $-0.005$ ,  $-0.001$ ,  $0.0$ ,  $0.0001$ ,  $0.0005$  and  $0.0009$

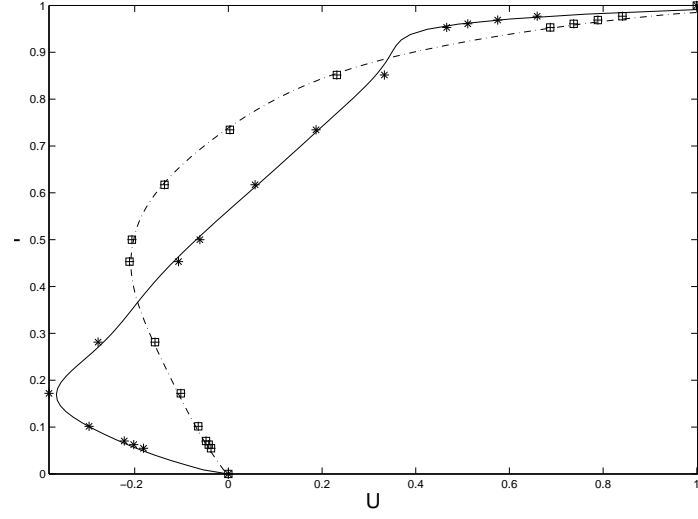


Figure 3.7. Centerline U-velocity for Reynolds numbers 100 and 1000. The dashed line is for  $Re = 100$  and the solid line is for  $Re = 1000$ .  $\boxplus$  and  $*$  are results of Ghia *et. al* [8] for  $Re = 100$  and 1000 respectively

Table 3.2. Strength and location of the centers of primary vortex for the lid-driven square cavity problem

Re		$\psi_{min}$	$x$	$y$
100	[8]	-0.103	0.6172	0.7344
	[4]	-0.103	0.6189	0.7400
	[20]	-0.103	0.6168	0.7375
	[21]	-0.103	0.6167	0.7417
	[22]	-0.103	0.6196	0.7373
	[5]	-0.103	0.6125	0.7375
	[Present]	-0.102	0.6125	0.7408
1000	[8]	-0.118	0.5313	0.5625
	[4]	-0.117	0.5335	0.5639
	[20]	-0.117	0.5438	0.5625
	[21]	-0.116	0.5286	0.5643
	[22]	-0.118	0.5333	0.5647
	[5]	-0.117	0.5250	0.5625
	[Present]	-0.119	0.5439	0.5634

Polar cavity flow is a well known test case for codes that has been written in curvilinear coordinates. A Newtonian, i.e.  $n = 1$ , laminar polar cavity flow at  $Re = 60$  and  $Re = 350$  is considered to test the accuracy of the present numerical method in curvilinear coordinates. The Reynolds number is based on the tangential velocity of the lid and the radius of curvature of the lid. The polar cavity is schematically shown in Figure 3.3. The flow domain is discretized by  $121 \times 121$  grid points. The Dirichlet boundary condition for velocities was prescribed at all boundaries. The solution reached steady state when the dimensionless time  $t = 20$ .

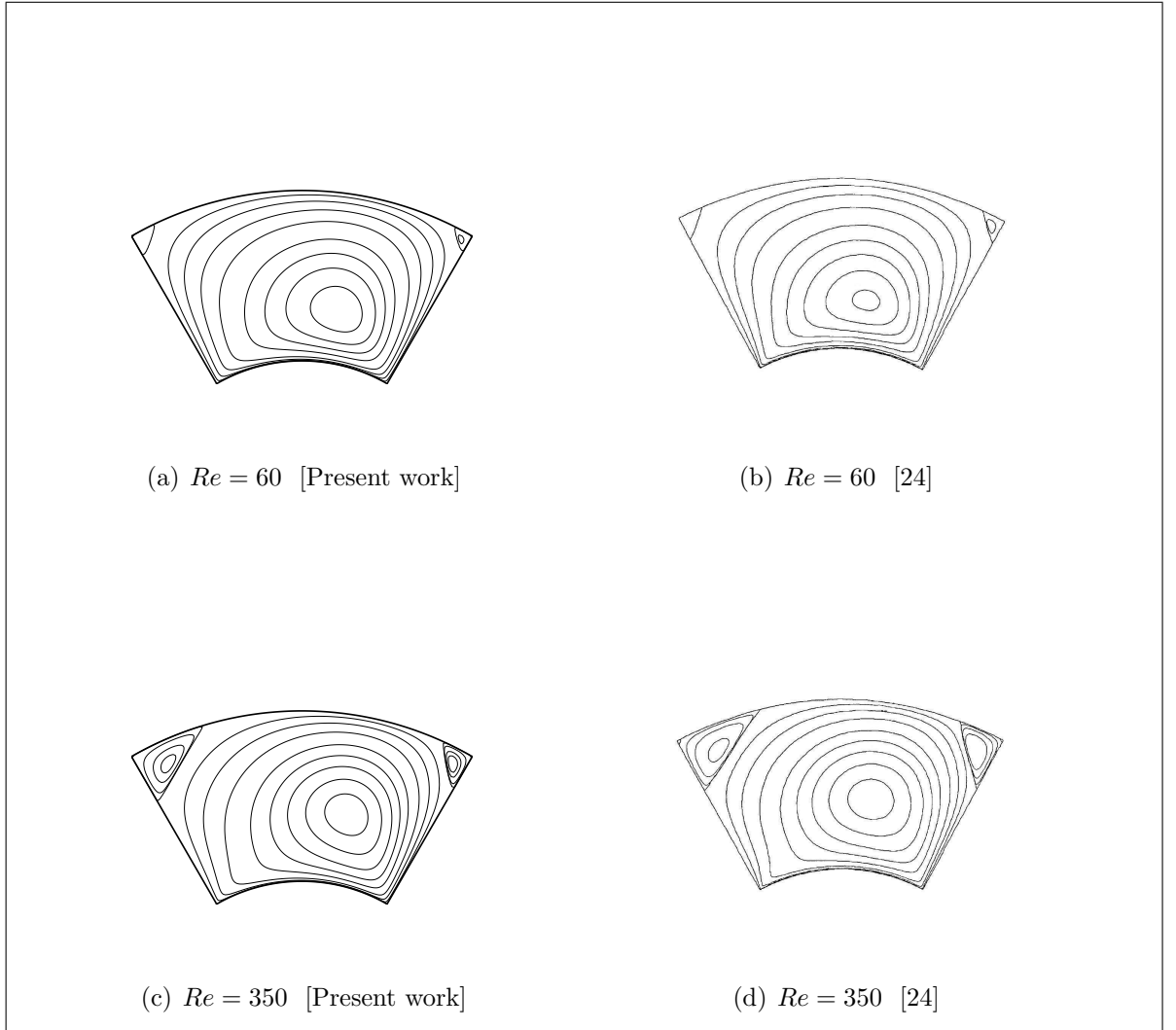


Figure 3.8. Comparison of Newtonian results of polar cavity for  $Re = 60$  and  $Re = 350$ . The streamline value equals 0 on the cavity boundary and contour levels shown for each plot are from the inner most contour  $-0.111$ ,  $-0.095$ ,  $-0.075$ ,  $-0.055$ ,  $-0.035$ ,  $-0.015$ ,  $-0.005$ ,  $-0.001$ ,  $0.0$ ,  $0.0001$ ,  $0.0005$  and  $0.0009$

The calculated streamline contours are shown in Figure 3.8(a) and 3.8(c) for  $Re = 60$  and  $Re = 350$  respectively. It can be seen in the Figure 3.8 that both computational results are in good agreement with the literature [24].

The Newtonian case, i.e.  $n = 1$ , for arc-shaped geometry is solved for  $Re = 100$ ,  $Re = 1000$  and  $Re = 1500$  with the aforementioned numerical technique and good results have been obtained. The Reynolds number is based on the lid velocity and the length of the lid. The arc cavity is schematically shown in Figure 3.4. The flow domain is discretized by  $61 \times 61$  grid points and the orthogonality conditions have been satisfied for both the stationary arc and the moving upper lid. The solution reached steady state when the dimensionless time  $t = 20$ .

The results obtained for  $Re = 100$ , 500 and 1000 can be seen in Figure 3.9(a), 3.9(c) and 3.9(e) respectively. Table 3.3 tabulates the maximum and the minimum streamline values for  $Re = 100$ ,  $Re = 1000$  and  $Re = 1500$  along with similar result found in literature [26].

Table 3.3. Strength of the maximum and minimum vortices for the lid-driven arc-shape cavity problem

Re		$\psi_{min}$	$\psi_{max}$
100	[26]	-0.0415832	0.0
	[Present ]	-0.051261	0.0
1000	[26]	-0.0450499	0.0001003
	[Present]	-0.0550949	0.0002553
1500	[26]	-0.0437994	0.0016739
	[Present]	-0.060935	0.00172326



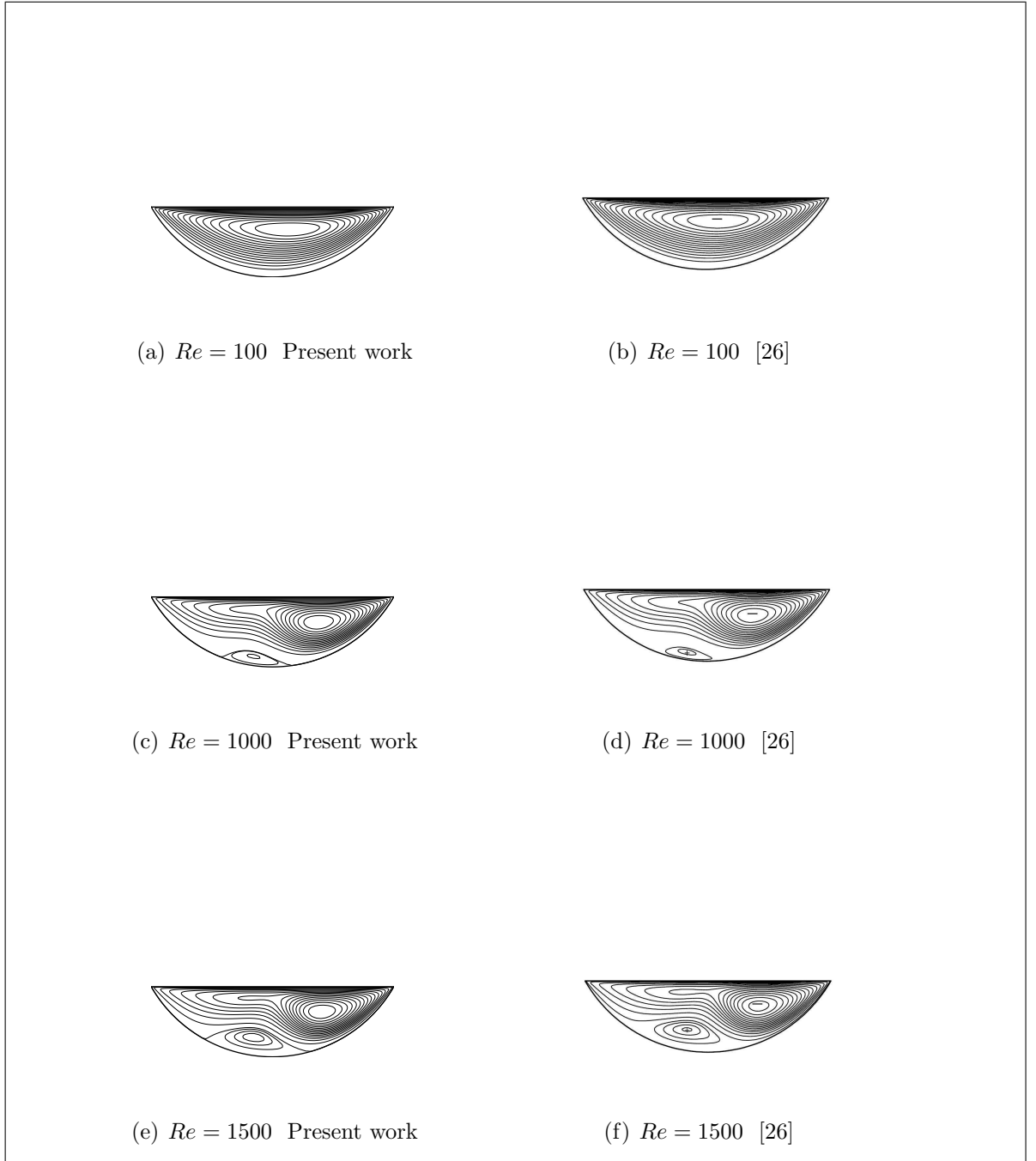


Figure 3.9. Comparison of Newtonian results of arc cavity for  $Re = 100, Re = 1000$  and  $Re = 1500$ . The streamline value equals 0 on the cavity boundary

## 4. RESULTS

Numerical solutions have been obtained for Reynolds number  $Re_{PL} = 100$ ,  $Re_{PL} = 1000$  for square geometry,  $Re_{PL} = 100$ ,  $Re_{PL} = 1000$  and  $Re_{PL} = 1700$  for polar geometry and  $Re_{PL} = 100$ ,  $Re_{PL} = 500$ ,  $Re_{PL} = 1000$  and  $Re_{PL} = 1500$  for arc geometry. For each Reynolds number computations were carried out for various values of the Power-Law index,  $n$ . The flow is completely characterized by the parameters  $Re_{PL}$  and  $n$ . The initial guess is the same for all flow conditions and it is chosen as the starting up flow. To determine the appropriate grid size several runs were performed with different values of grid size. It is found that the  $81 \times 81$  grid is a good choice for square cavity with a clustering parameter 1.1 near the walls for all Reynolds numbers used in this study. It is also found  $121 \times 121$  grid is adequate for polar cavity and  $61 \times 61$  grid is adequate for arc -shaped cavity.

Similarity in non-Newtonian flows of a certain model is achieved when all parameters derived from the non-dimensionalisation procedure are the same [16]. Following the non-dimensionalisation procedure described in Section (2.1) and (2.2) one can conclude that the parameters upon which similarity depends are:  $Re_{PL}$  and  $n$  for the Power-Law model which reduces to Newtonian case when  $n$  is equal to 1. Therefore the non-Newtonian effects of the aforementioned model can be studied by investigating the flow effects caused by changing the values of these parameters.

In order to investigate the effects of non-Newtonian parameters Power-Law model is used for three cavity geometries: square cavity, polar cavity and arc-shaped cavity. It is important to stress out that the first geometry is a planar geometry where the grid orthogonality is satisfied automatically whereas the second and the third geometries are curved and it is relatively harder to achieve an orthogonal grid for the arc-shape cavity.

The streamline patterns of the square geometry for  $Re_{PL} = 100$  are shown in Figure 4.1 for  $n$  values varying from 0.75 to 1.5. For  $Re_{PL} = 100$  Figures 4.2(e), 4.2(a) and 4.1(c) are for  $n = 0.75$ ,  $n = 1$  and  $n = 1.5$  respectively. As can be seen from the figure as Power-Law index  $n$  decreased the corner vortices vanished and as the Power-Law index  $n$  increased the corner vortices became bigger.

The corner vortices have been investigated in detail for shear thinning case where  $n < 1$ . For that purpose several  $n$  values are examined in Figure 4.2 for which the corner vortices show weakening and finally vanish. Table 4.1 tabulates the maximum strength of corner vortices for  $n = 0.75$ ,  $n = 0.8$ ,  $n = 0.85$ ,  $n = 0.9$  and finally  $n = 1$ . It is clear that as the Power-Law index  $n$  gets smaller because of the shear thinning effect the intensity of the corner vortices diminish.

Table 4.1. Strength of the maximum corner vortices for the lid-driven square cavity problem for  $Re_{PL} = 100$  for various  $n$  values

$Re_{PL} = 100$	$\psi_{max}$
$n = 1.0$	0.0000135
$n = 0.90$	0.00000235
$n = 0.85$	0.00000041
$n = 0.80$	0.00000001
$n = 0.75$	0.0

The streamline patterns of the square geometry for  $Re_{PL} = 1000$  are shown in Figure 4.3 for  $n$  values varying from 0.75 to 1.5. For  $Re_{PL} = 1000$  Figures 4.3(a), 4.3(b) and 4.3(c) are for  $n = 0.75$ ,  $n = 1$  and  $n = 1.5$  respectively. In shear thinning case i.e.  $n = 0.75$  the corner vortices became smaller whereas in the shear thickening case i.e.  $n = 1.5$  the intensity of the right and left corner vortices equalized compared to the Newtonian case i.e  $n = 1$ .

Transient variation of the flow field is displayed in Figure 4.4 for the case at  $Re_{PL} = 1000$  and  $n = 1.5$  at non-dimensional time levels  $t = 1$ ,  $t = 5$ ,  $t = 10$ ,  $t = 15$ ,  $t = 20$ . For this case, the steady state is reached approximately at  $t \sim 15$ . As can be seen from the figure, the primary vortex core is almost moving along the square cavity diagonal line. The change of the horizontal component of the velocity (i.e.  $u$ ) at point  $(0.135; 0.135)$  in time is shown in Figure 4.5(a). The value of  $u$  converges approximately to 0.019.

In order to demonstrate the convergence of the solution to steady state we calculate the relative error norm (REN) of the vorticity at each  $(k + 1)^{th}$  Adams-Bashforth iteration as

$$REN = \sqrt{\frac{\sum_{i,j=1}^{N_x, N_y} (\Omega_{i,j}^{k+1}(i) - \Omega_{i,j}^k(i))^2}{\sum_{i,j=1}^{N_x, N_y} \Omega_{i,j}^{k+1}(i)^2}} \quad (4.1)$$

where  $N_x$  and  $N_y$  denote the number of grid points in the  $x$  and  $y$  directions respectively. Figure 4.5(b) shows a log-log scale of REN versus the number of iterations at  $Re_{PL} = 1000$  and  $n = 1.5$ . The figure shows an exponential decay on REN which is close to  $4.5 \times 10^{-8}$  after 300000 Adams-Bashforth iterations.

Due to the numerical restrictions, we fixed our parameter range to  $0.75 < n < 1.2$ . Although aforementioned range is close to the Newtonian case it is possible to draw conclusions about the shear thinning and shear thickening effects. The streamline patterns of the polar cavity for  $Re_{PL} = 100$  are shown in Figure 4.6 for  $n$  values varying from 0.75 to 1.2. For  $Re_{PL} = 100$  Figures 4.6(a), 4.6(b) and 4.6(c) are for  $n = 0.75$ ,  $n = 1$  and  $n = 1.2$  respectively. Both in shear thinning and shear thickening cases the vortex core moved to the polar cavity center and the upper left corner vortex became bigger.

The streamline patterns of the polar cavity for  $Re_{PL} = 1000$  are shown in Figure 4.7 for  $n$  values varying from 0.75 to 1.2. The movement of the lower lid lead to the onset of a *contour-clockwise* vortex core where the corner vortices are rotating in opposite direction. For  $Re_{PL} = 1000$  when  $n = 1$  the primary vortex is rotating in *contour-clockwise* direction whereas the upper corner vortices are rotating in the *clockwise* direction. In shear thinning case, i.e.  $n = 0.75$ , this fact does not change, but the upper right vortex pushes the primary vortex and gets bigger where the upper left vortex gets smaller. However in shear thickening case at  $Re_{PL} = 1000$  with  $n = 1.2$  an upper left secondary vortex is observed to rotate in a *contour-clockwise* direction where the other vortices are rotating in the same direction, i.e. the primary vortex in *contour-clockwise* direction and upper left and right vortices in *clockwise* direction (See Figure 4.8 for details). Additionally in shear thickening case the central vortex moves to the center of the cavity and both left and right upper vortices get bigger.

The streamline patterns of the polar cavity for  $Re_{PL} = 1700$  are shown in Figure 4.9 for  $n$  values varying from 0.75 to 1.2. For  $Re_{PL} = 1700$  when  $n = 1$  the left corner vortex became dominant. In shear thinning case, i.e.  $n = 0.75$ , left corner vortex moved downwards and pushed the primary vortex and the right corner vortex got smaller. The directions of vortices are not changed for Newtonian and the shear thinning cases. However in shear thickening case at  $Re_{PL} = 1700$  with  $n = 1.2$  an upper left secondary vortex is observed to rotate in a *contour-clockwise* direction where the primary vortex in *contour-clockwise* direction and upper left and right vortices in *clockwise* direction. Additionally in shear thickening case the central vortex is moved to the center of the cavity. The upper left vortex is bigger whereas the upper right vortex is not changed.

Displayed in Table 4.2 are maximum and minimum values of streamlines of arc cavity for  $Re_{PL} = 100, 500, 1000$  and  $1500$  and various values of  $n$ . For each case, minimum and maximum values of the streamlines within the solution domain are provided for a quantitative comparison.

Table 4.2. Strength of the maximum and minimum vortices for the lid-driven arc-shape cavity problem for  $Re_{PL} = 100$ ,  $Re_{PL} = 500$ ,  $Re_{PL} = 1000$  and  $Re_{PL} = 1500$  for various  $n$  values

$Re_{PL}$		$\psi_{min}$	$\psi_{max}$
100	$n = 0.75$	-0.057202	0.0
	$n = 1$	-0.051261	0.0
	$n = 1.2$	-0.049009	0.0
500	$n = 0.75$	-0.0391821	0.0
	$n = 1$	-0.0616643	0.0
	$n = 1.2$	-0.0422601	0.0
1000	$n = 0.75$	-0.0632133	0.000025938
	$n = 1$	-0.0550949	0.0002553
	$n = 1.2$	-0.0547259	0.000422858
1500	$n = 0.75$	-0.0698844	0.00000359
	$n = 1$	-0.060935	0.00172326
	$n = 1.2$	-0.0549559	0.00174505

The streamline patterns of the arc-shaped cavity for  $Re_{PL} = 100$  and  $Re_{PL} = 500$  are shown in Figure 4.10, 4.11 for  $n$  values varying from 0.75 to 1.2. For  $Re_{PL} = 100$  Figures 4.10(a), 4.10(b) and 4.10(c) and 4.11(a), 4.11(b) and 4.11(c) are for  $n = 0.75$ ,  $n = 1$  and  $n = 1.2$  respectively. For both shear thinning, i.e.  $n = 0.75$ , and shear thickening, i.e.  $n = 1.2$ , only the contour levels are changed, the characteristic of the flow is not changed in appreciable amount.

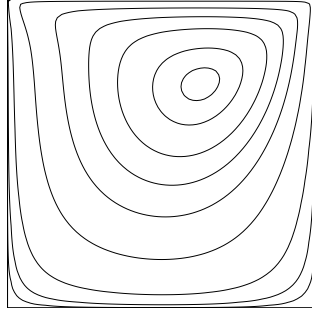
The streamline patterns of the arc-shaped cavity for  $Re_{PL} = 1000$  are shown in Figure 4.12 for  $n$  values varying from 0.75 to 1.2. For  $Re_{PL} = 1000$  Figures 4.12(a), 4.12(b) and 4.12(c) are for  $n = 0.75$ ,  $n = 1$  and  $n = 1.2$  respectively. For  $Re_{PL} = 1000$  in Newtonian case, i.e.  $n = 1$ , a secondary vortex is observed at the bottom of the cavity. As the movement of the flat lid leads to the formation of a main vortex cell rotating in the *counter-clockwise* direction whereas the secondary vortex is rotating in the *clockwise* direction. Both in shear thinning and shear thickening cases this fact is

not changed. In shear thinning case, i.e.  $n = 0.75$ , the secondary vortex is smaller so that it almost vanishes. However in shear thickening case at  $Re_{PL} = 1000$  with  $n = 1.2$  the lower secondary vortex is bigger and pushes the main vortex core upwards and the center of the secondary vortex moves to left.

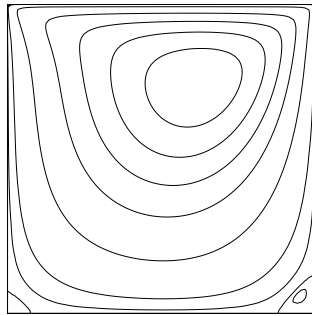
Transient variation of the flow field for arc shape cavity is displayed in Figure 4.13 for the case at  $Re_{PL} = 1000$  and  $n = 1.2$  at non-dimensional time levels  $t = 1$ ,  $t = 5$ ,  $t = 10$ ,  $t = 15$ ,  $t = 20$ . As can be seen from the figure, the primary vortex core is moving to the center of the arc cavity. The secondary vortex is appears almost at dimensionless time  $t = 5$  and develops. For this case, the steady state is reached approximately at  $t \sim 12.5$ . The change of the horizontal component of the velocity (i.e.  $u$ ) at point  $(0.135; -0.135)$  in time is shown in Figure 4.14(a). The value of  $u$  converges approximately to 0.09.

In order to demonstrate the convergence of the solution to steady state we calculate the relative error norm (REN) of the vorticity at each  $(k + 1)^{th}$  Adams-Bashforth iteration as described in Equation (4.1). Figure 4.14(b) shows a log-log scale of REN versus the number of iterations at  $Re_{PL} = 1000$  and  $n = 1.2$ . The figure shows an exponential decay on REN which is close to  $5 \times 10^{-10}$  after 500000 Adams-Bashforth iterations. The peaks in that figure is caused by the highly non-linear nature of the vorticity transport equation.

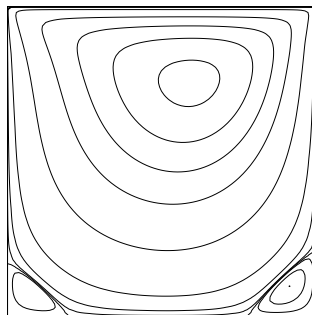
The streamline patterns of the arc-shaped cavity for  $Re_{PL} = 1500$  are shown in Figure 4.15 for  $n$  values varying from 0.75 to 1.2. For  $Re_{PL} = 1500$  Figures 4.15(a), 4.15(b) and 4.15(c) are for  $n = 0.75$ ,  $n = 1$  and  $n = 1.2$  respectively. For  $Re_{PL} = 1500$  in Newtonian case a secondary vortex is observed at the bottom of the cavity. In shear thinning case, i.e.  $n = 0.75$ , the secondary vortex is smaller so that it almost vanishes. However in shear thickening case at  $Re_{PL} = 1500$  with  $n = 1.2$  the lower secondary vortex is bigger and pushes the main vortex core upwards and the center of the secondary vortex moves to left.



(a)  $Re_{PL} = 100, n = 0.75$



(b)  $Re_{PL} = 100, n = 1$



(c)  $Re_{PL} = 100, n = 1.5$

Figure 4.1. Effects of Power-Law index  $n$  on the stream line contours for  $Re_{PL} = 100$ .

The streamline value equals 0 on the cavity boundary and contour levels shown for each plot are in the interval  $(-0.11) - (0.01)$



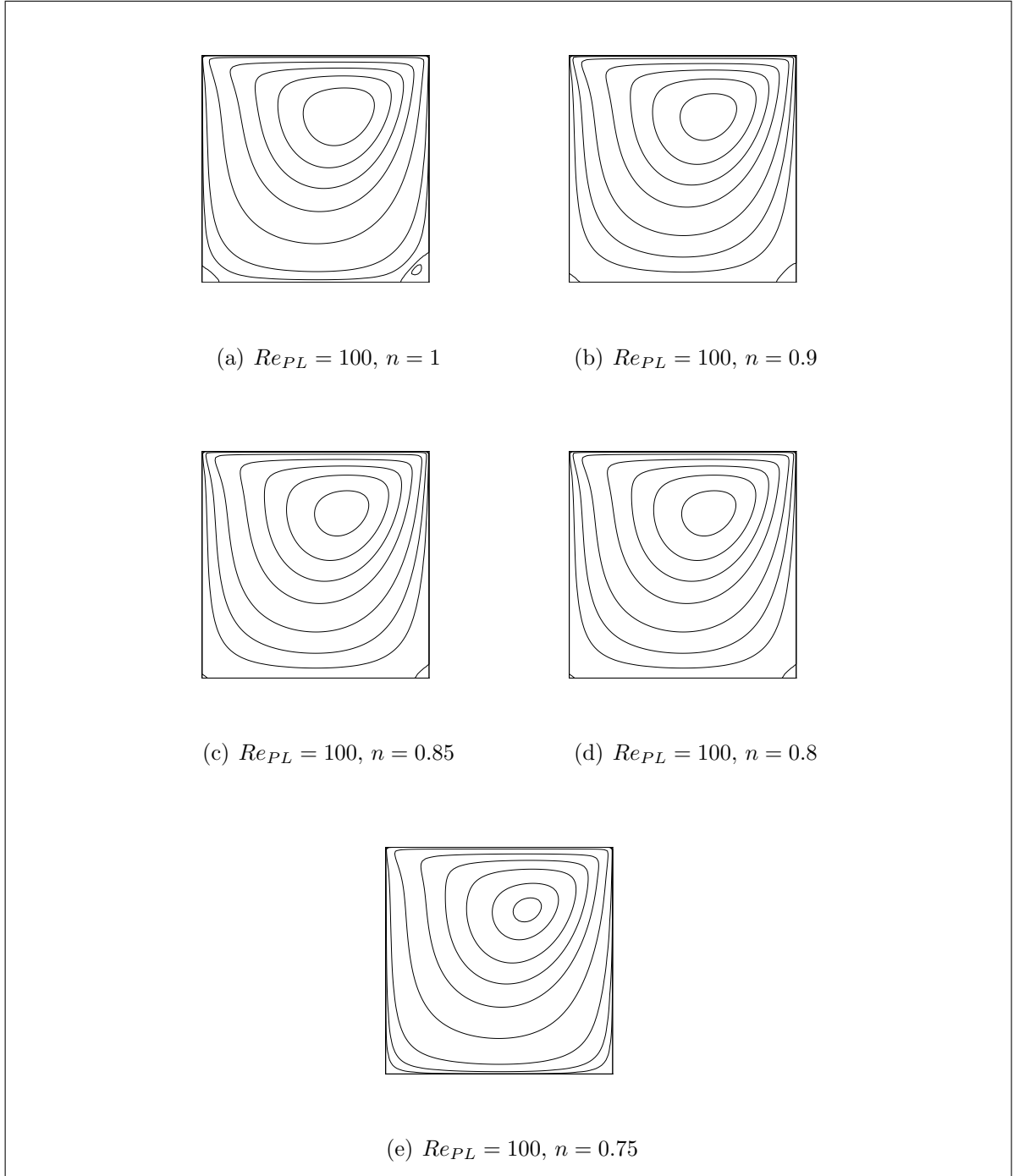
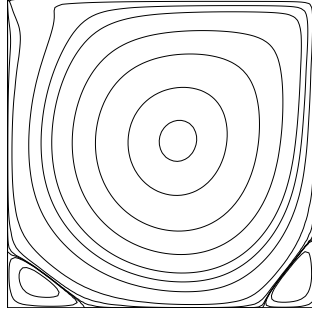
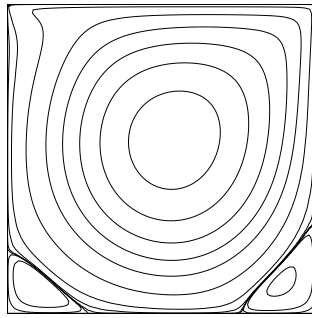


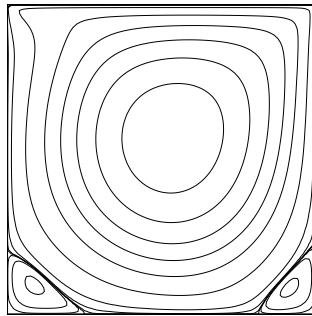
Figure 4.2. Shear thinning effect of Power-Law index  $n$  on the stream line contours for  $Re_{PL} = 100$ . The streamline value equals 0 on the cavity boundary and contour levels shown for each plot are in the interval  $(-0.11) - (0.01)$



(a)  $Re_{PL} = 1000$ ,  $n = 0.75$



(b)  $Re_{PL} = 1000$ ,  $n = 1$



(c)  $Re_{PL} = 1000$ ,  $n = 1.5$

Figure 4.3. Effects of Power-Law index  $n$  on the stream line contours for  $Re_{PL} = 1000$ . The streamline value equals 0 on the cavity boundary and contour levels shown for each plot are in the interval  $(-0.11) - (0.0009)$

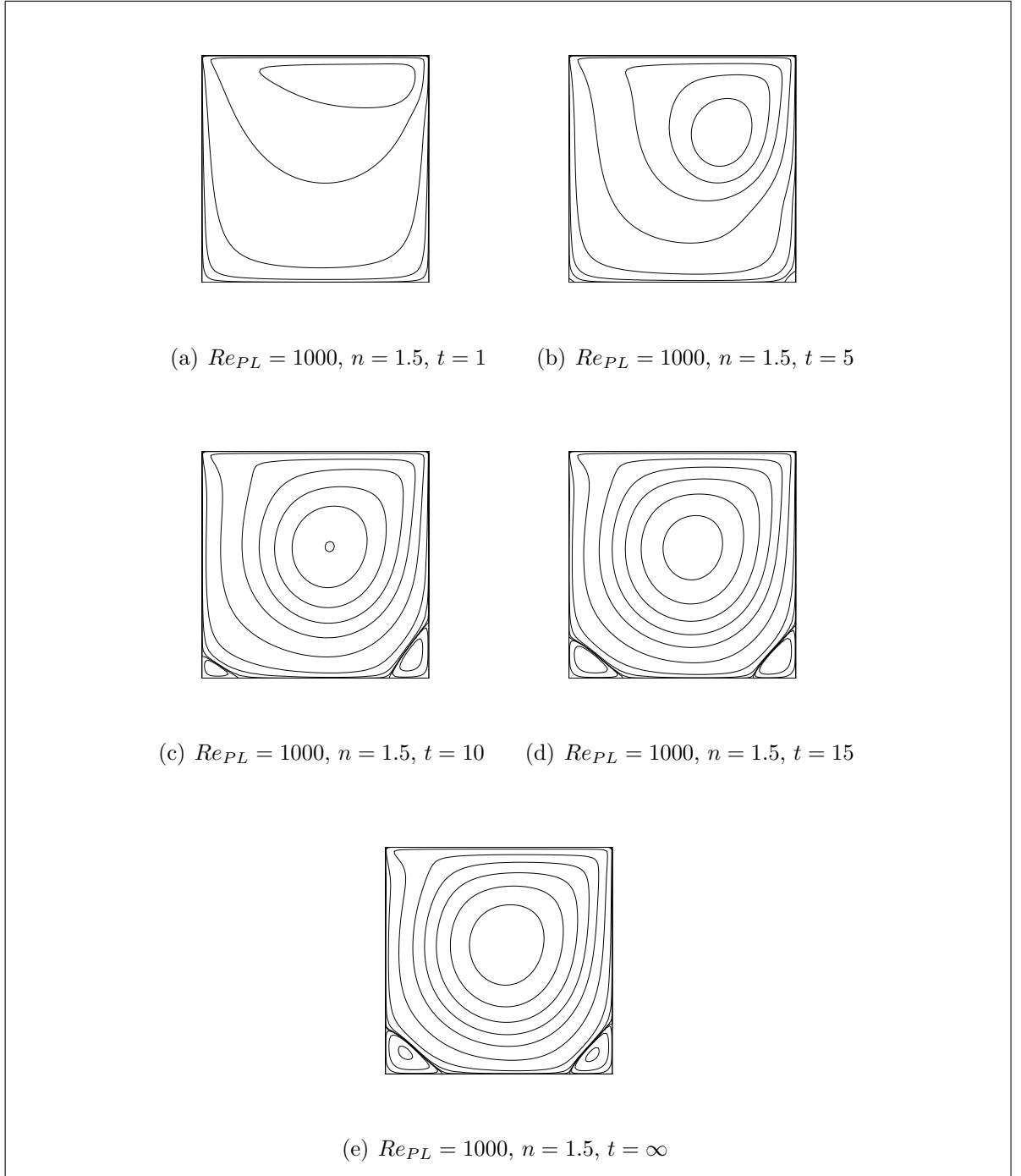
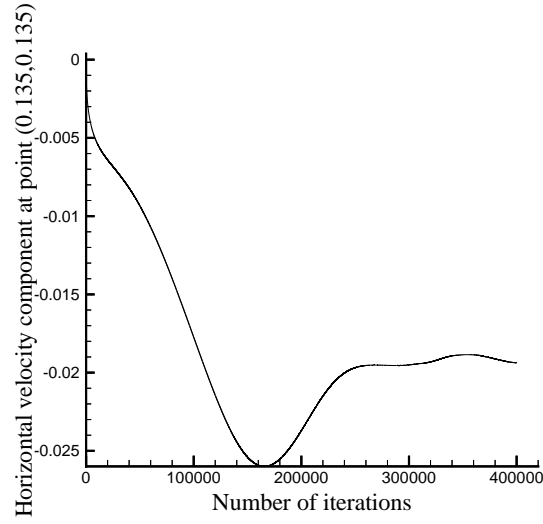
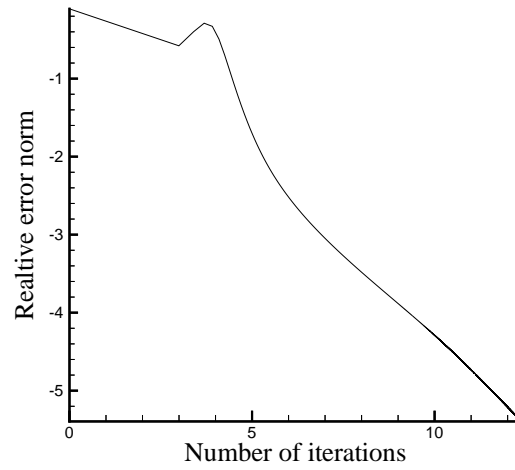


Figure 4.4. Transient variation of the flow field for  $Re_{PL} = 1000$  and  $n = 1.5$ . The streamline value equals 0 on the cavity boundary and contour levels shown for each plot are in the interval  $(-0.11) - (0.0009)$

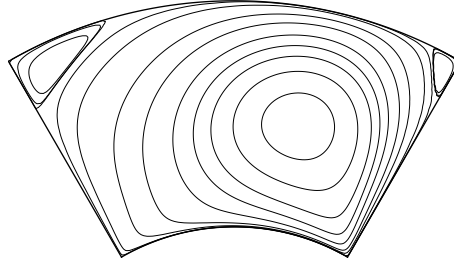


(a)  $Re_{PL} = 1000$ ,  $n = 1.5$  Horizontal velocity at point (0.135;0.135) vs. number of iterations

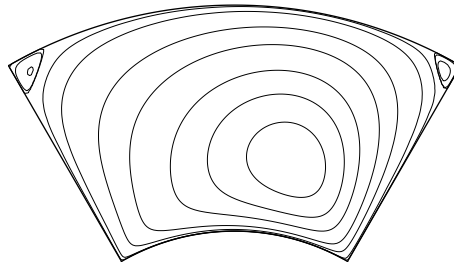


(b)  $Re_{PL} = 1000$ ,  $n = 1.5$  Logarithm of Relative error norm vs. logarithm of number of iterations

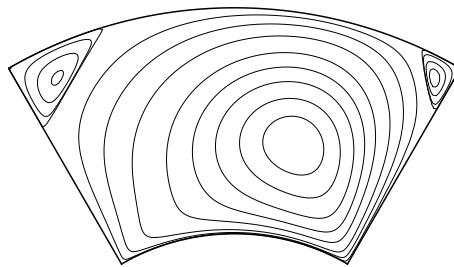
Figure 4.5. Convergence plots for  $Re_{PL} = 1000$  and  $n = 1.5$



(a)  $Re_{PL} = 100, n = 0.75$



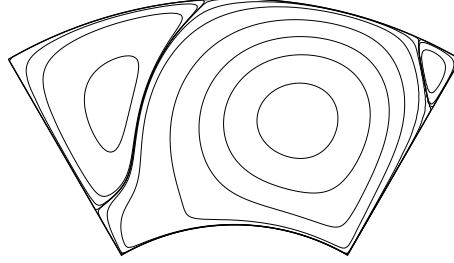
(b)  $Re_{PL} = 100, n = 1$



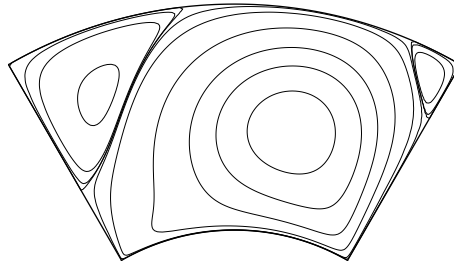
(c)  $Re_{PL} = 100, n = 1.2$

Figure 4.6. Effects of Power-Law index  $n$  on the stream line contours for  $Re_{PL} = 100$ .

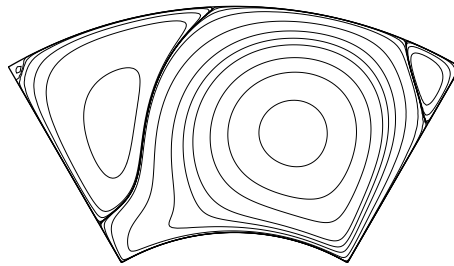
The streamline value equals 0 on the cavity boundary and contour levels shown for each plot are in the interval  $(-0.25) - (0.00001)$



(a)  $Re_{PL} = 1000, n = 0.75$

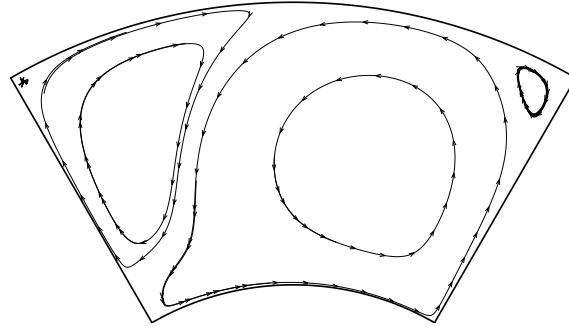


(b)  $Re_{PL} = 1000, n = 1$

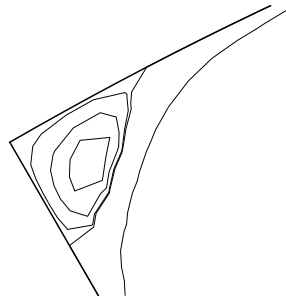


(c)  $Re_{PL} = 1000, n = 1.2$

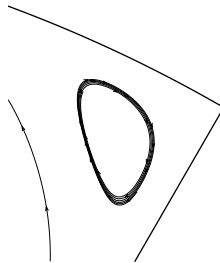
Figure 4.7. Effects of Power-Law index  $n$  on the stream line contours for  $Re_{PL} = 1000$ . The streamline value equals 0 on the cavity boundary and contour levels shown for each plot are in the interval  $(-0.25) - (0.00001)$



(a)  $Re_{PL} = 1000$ ,  $n = 1.2$

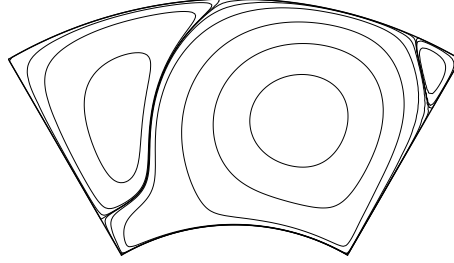


(b)  $Re_{PL} = 1000$ ,  $n = 1.2$  upper left corner secondary vortex detail

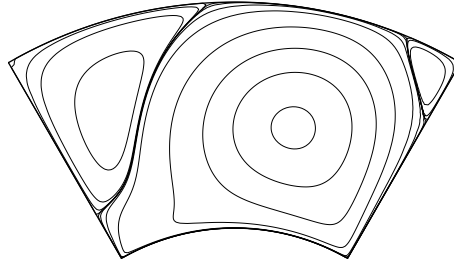


(c)  $Re_{PL} = 1000$ ,  $n = 1.2$  upper right corner vortex detail

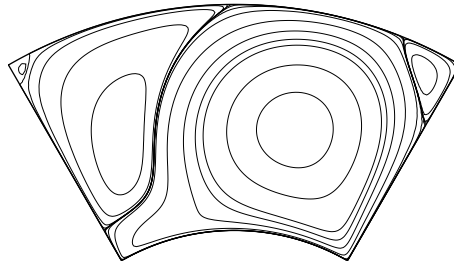
Figure 4.8. Directions of vortices for  $Re_{PL} = 1000$  and  $n = 1.2$



(a)  $Re_{PL} = 1700, n = 0.75$



(b)  $Re_{PL} = 1700, n = 1$



(c)  $Re_{PL} = 1700, n = 1.2$

Figure 4.9. Effects of Power-Law index  $n$  on the stream line contours for  $Re_{PL} = 1700$ . The streamline value equals 0 on the cavity boundary and contour levels shown for each plot are in the interval  $(-0.25) - (0.00001)$



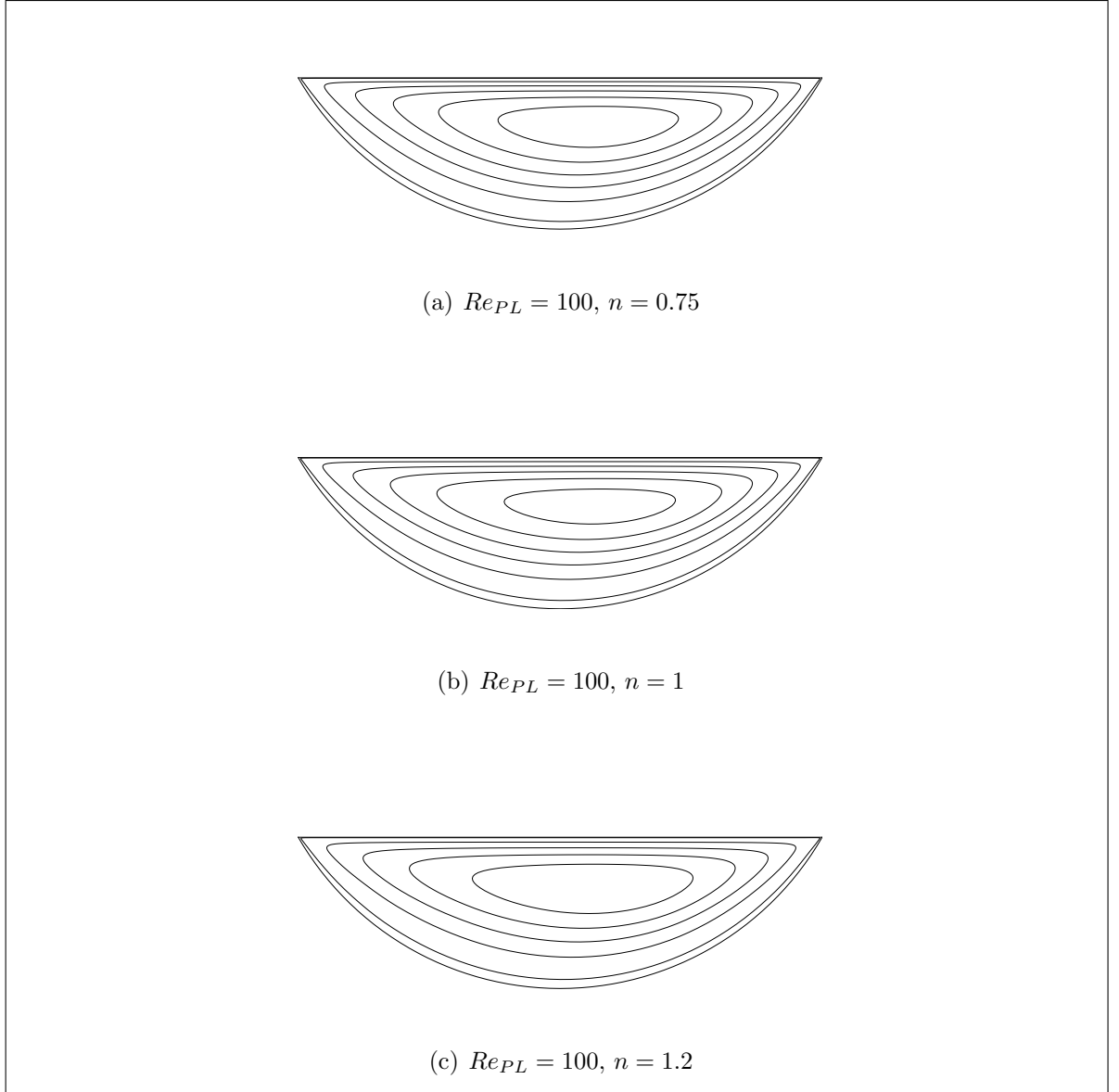


Figure 4.10. Effects of Power-Law index  $n$  on the stream line contours for  $Re_{PL} = 100$ . The streamline value equals 0 on the cavity boundary and contour levels shown for each plot are in the interval  $(-0.055) - (0.0002)$

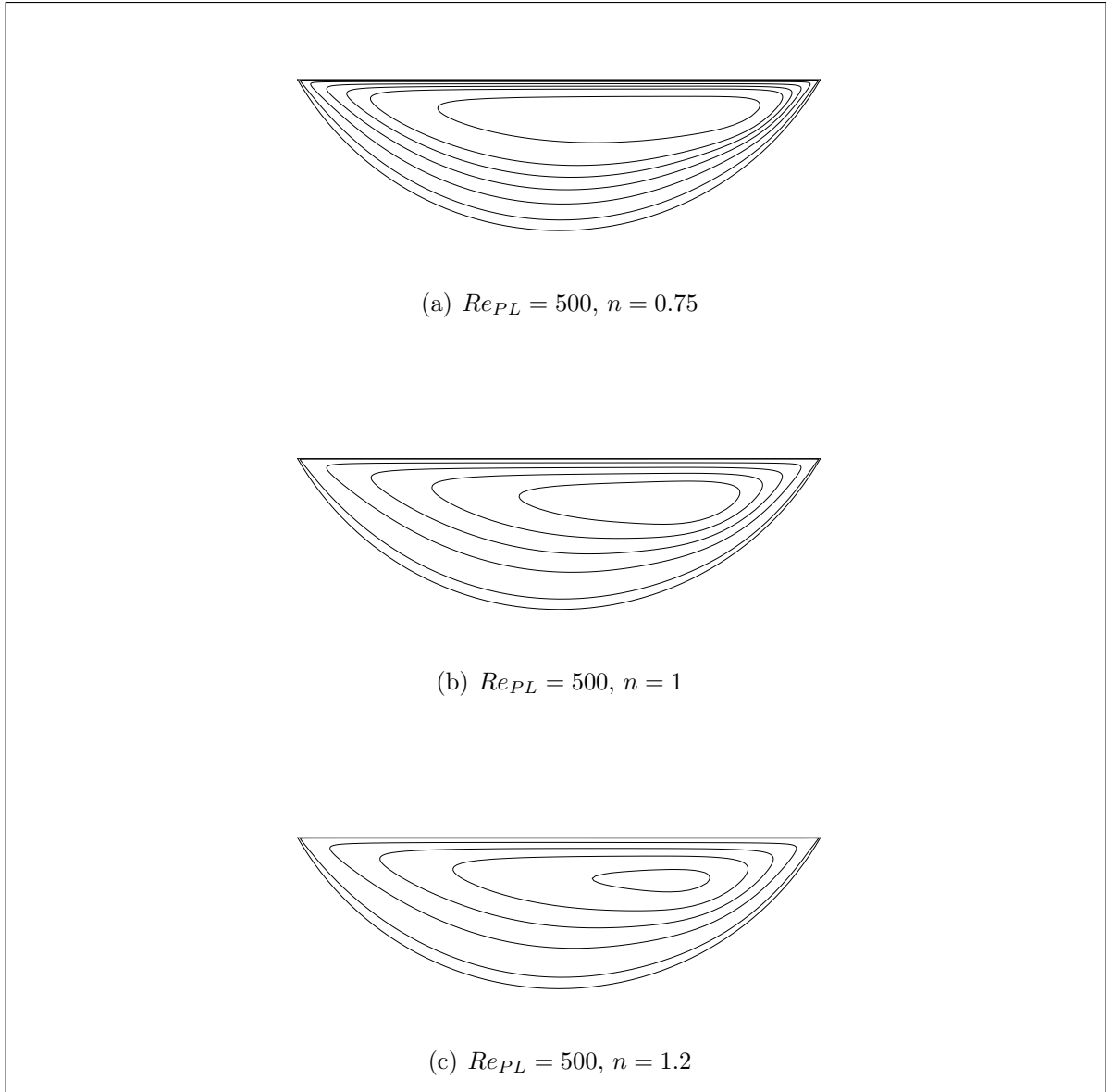


Figure 4.11. Effects of Power-Law index  $n$  on the stream line contours for  $Re_{PL} = 500$ . The streamline value equals 0 on the cavity boundary and contour levels shown for each plot are in the interval  $(-0.055) - (0.0002)$

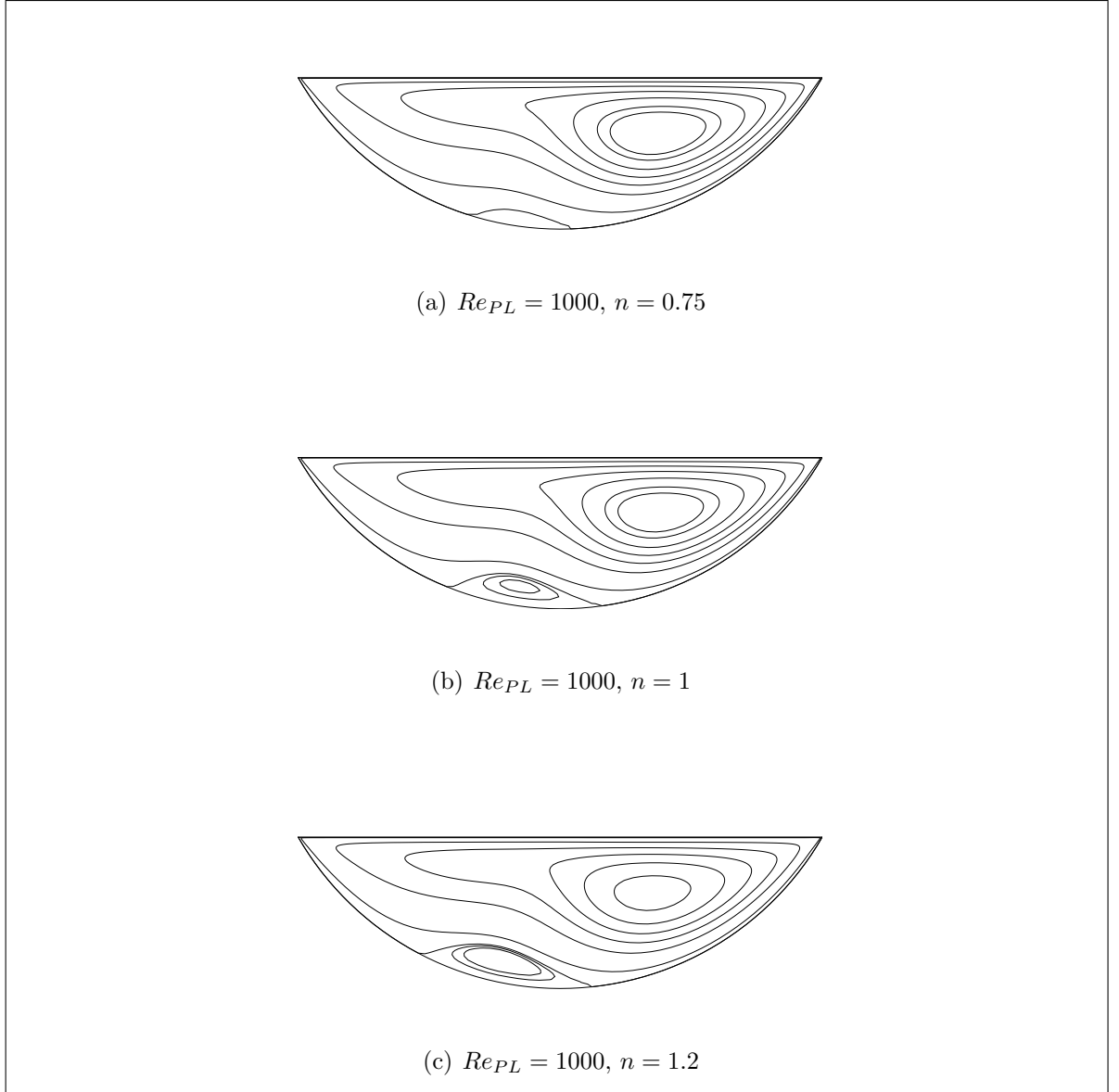


Figure 4.12. Effects of Power-Law index  $n$  on the stream line contours for  $Re_{PL} = 1000$ . The streamline value equals 0 on the cavity boundary and contour levels shown for each plot are in the interval  $(-0.055) - (0.0002)$

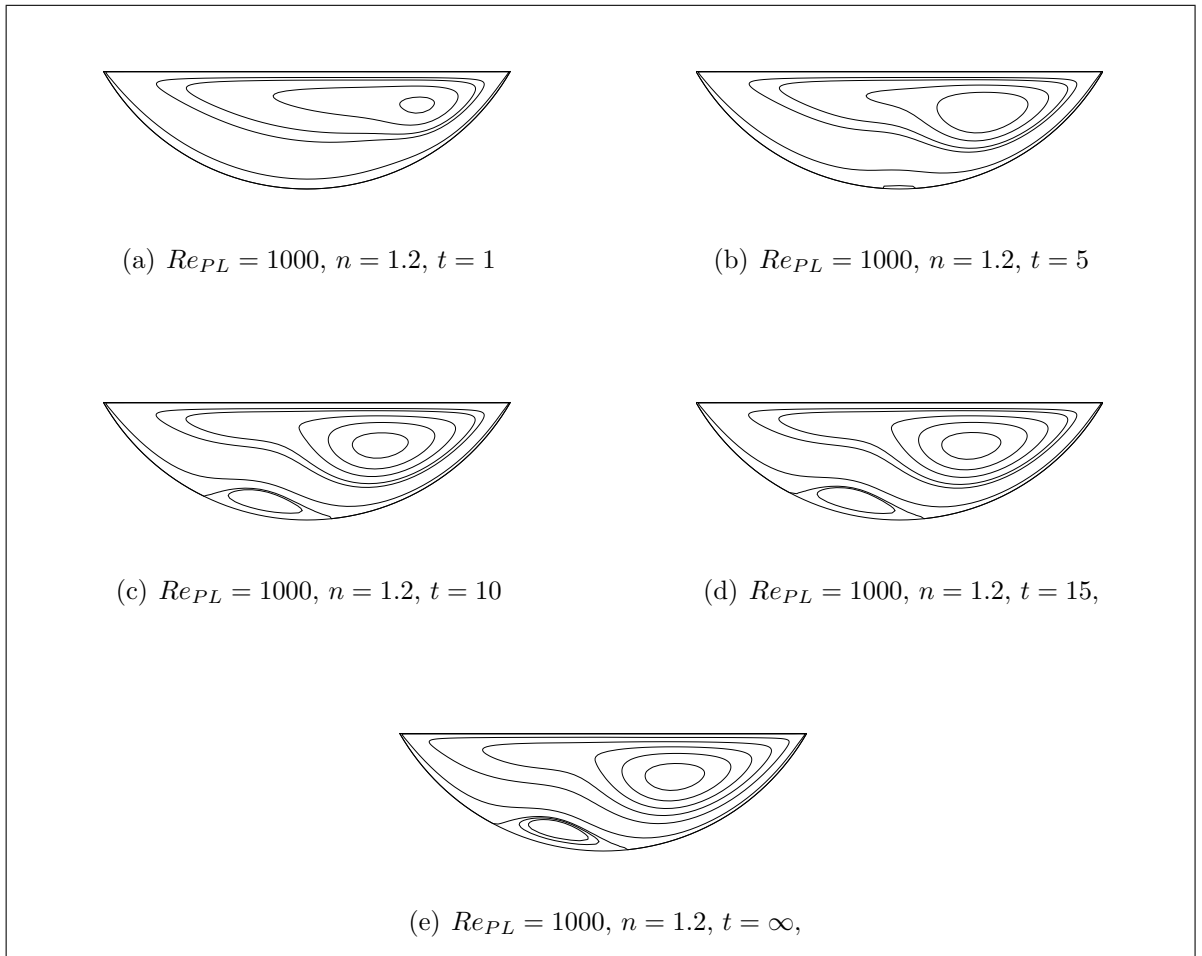
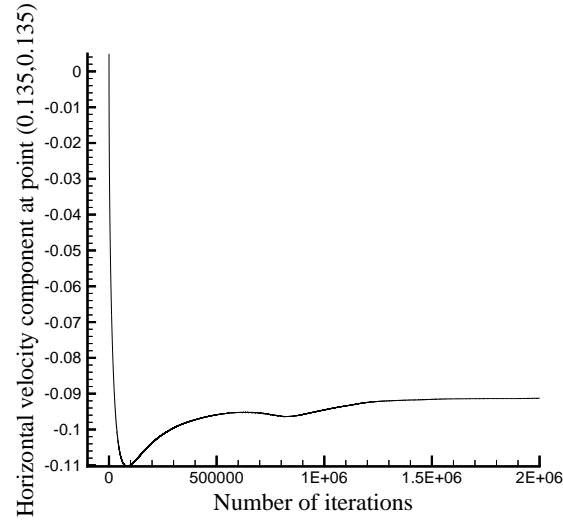
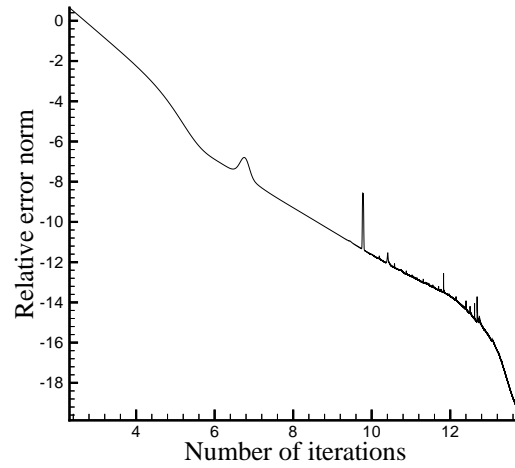


Figure 4.13. Time evolution of arc shape cavity for  $Re_{PL} = 1500, n = 1.2$



(a)  $Re_{PL} = 1000$ ,  $n = 1.2$  Horizontal velocity at point  $(0.135; -0.135)$  vs. number of iterations



(b)  $Re_{PL} = 1000$ ,  $n = 1.2$  Logarithm of Relative error norm vs. logarithm of number of iterations

Figure 4.14. Convergence plots for arc shape cavity,  $Re_{PL} = 1000$  and  $n = 1.2$

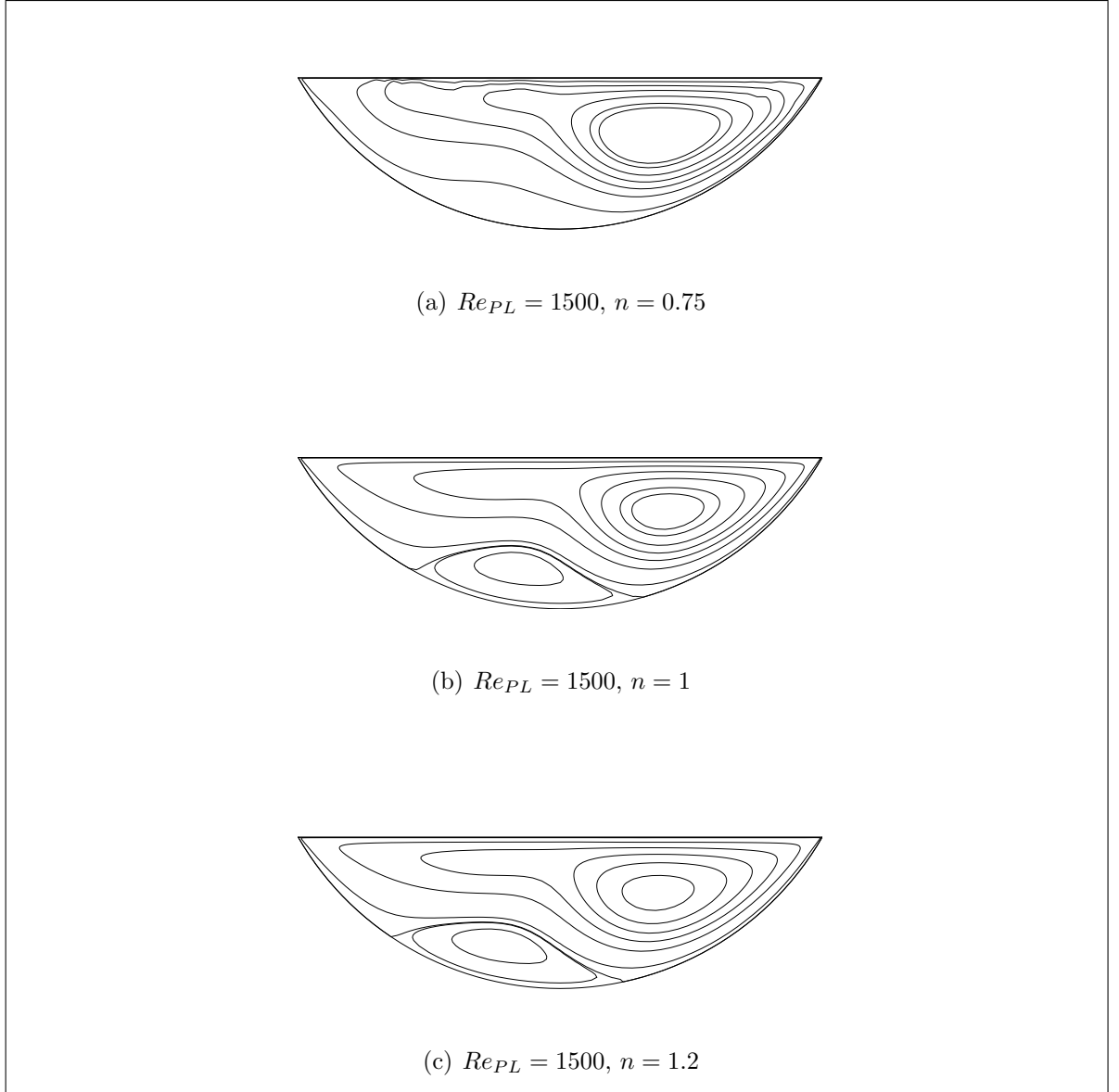


Figure 4.15. Effects of Power-Law index  $n$  on the streamline contours for  $Re_{PL} = 1500$ . The streamline value equals 0 on the cavity boundary and contour levels shown for each plot are in the interval  $(-0.055) - (0.0002)$

## 5. CONCLUSIONS

Numerical simulations on lid-driven cavity flows of Newtonian and non-Newtonian fluids are presented. The inelastic Power-Law fluid model has been chosen as the non-Newtonian constitutive relation. A finite difference method based on unsteady vorticity stream-function formulation has been applied in two dimensional plane and curved geometries. The main advantage of the present method lies in the elimination of the pressure term from the governing equations. For the accuracy of the numerical solution, the body-fitted coordinate system has been used such that the boundary conditions have been represented in a way that the boundary is coincident with some coordinate line.

It has also been shown that the present numerical method yields accurate computational results even when highly skewed, unequally spaced, curved grid were used. Equally importantly, the present method was found to be strongly convergent for high Reynolds number non-Newtonian flows as well as for flows with complex geometries.

Newtonian and non-Newtonian flow computations were performed using three different geometries, namely, lid-driven square cavity, lid-driven polar cavity and lid-driven arc-shape cavity. The code is validated against Newtonian lid-driven cavity flow cases for all geometries. Results from current study are in very good agreement with results by previous researchers for Newtonian flow case. Then, the code is used to obtain solutions for several Reynolds numbers with both shear thinning and shear thickening fluids.

It is observed that, for  $Re = 100$  and  $Re = 1000$ , in square cavity the intensity of lower left and lower right corner vortices are decreased in the shear thinning case. However in the shear thickening case they become more intensive compared to the Newtonian case.

In polar cavity flow the upper left corner vortex became more intensive in both shear thinning and shear thickening cases for all Reynolds number covered in that study, i.e.  $Re = 100$ ,  $Re = 1000$  and  $Re = 1700$ . For both high inertia cases, i.e.  $Re = 1000$  and  $Re = 1700$ , the primary vortex moved to the center of the cavity where the upper left corner vortex had more space to rotate. In addition to that growth, in high Reynolds numbers and in the shear thickening case a secondary upper left corner vortex is observed to rotate in the same direction with the primary vortex where the other vortices are observed to rotate in the opposite direction.

In arc-shaped cavity flow at relatively low Reynolds numbers, i.e.  $Re = 100$  and  $Re = 500$ , in both shear thinning and shear thickening cases the values of the streamlines are varied in a way that the minimum streamline value decreased as Power-Law index  $n$  decreased (See Table (4.2) for detail). At high Reynolds numbers, i.e.  $Re = 1000$  and  $Re = 1500$ , the secondary vortex is observed. The intensity of the bottom secondary vortex is decreased and finally the vortex is vanished in the shear thinning case, whereas, it is increased in the shear thickening case. In the shear thickening case, at high  $Re$  numbers, the center of the bottom secondary vortex is moved to upper left and pushed the primary vortex upwards.

It can be concluded that, for  $Re \leq 1000$ , when shear thinning effects are dominant intensity of the corner vortices are increased in square and arc cavity cases. For higher Reynolds numbers, in polar cavity, inertial forces appear to be effective in the growth of corner vortices compared to Newtonian case. Also, as shear thickening increased this growth becomes more appreciable. Additionally, as described above in detail, at high inertia regimes secondary vortices are observed.

As a future work, it may be interesting to study the non-Newtonian effects such as shear thinning and shear thickening in the low inertia regime. Also, it may be interesting to study the behavior of a viscoelastic fluid and observe the combined effect of inertia and elasticity on the formation of the vortices in plane and curved lid-driven cavity flows.



## APPENDIX A: TRANSFORMATIONS

In Cartesian coordinates the vorticity transport equation for Power-Law fluid is as:

$$\begin{aligned}
 I_2^{\frac{n-1}{2}} \left( \frac{\partial^2 \Omega}{\partial x^2} + \frac{\partial^2 \Omega}{\partial y^2} \right) &+ \frac{(n-1)}{2} I_2^{\frac{n-3}{2}} \left( \frac{\partial I_2}{\partial y} \frac{\partial \Omega}{\partial y} + \frac{\partial I_2}{\partial x} \frac{\partial \Omega}{\partial x} \right) \\
 &- \frac{(n-1)(n-3)}{2} I_2^{\frac{n-5}{2}} \left( G_1 \frac{\partial I_2}{\partial y} - G_2 \frac{\partial I_2}{\partial x} \right) \\
 &- (n-1) I_2^{\frac{n-3}{2}} \left( \frac{\partial G_1}{\partial y} - \frac{\partial G_2}{\partial x} \right) = Re_{PL} \left( \frac{\partial \Omega}{\partial t} + u \frac{\partial \Omega}{\partial x} + v \frac{\partial \Omega}{\partial y} \right)
 \end{aligned} \tag{A.1}$$

where

$$G_1 = \frac{\partial I_2}{\partial x} \frac{\partial u}{\partial x} + \frac{1}{2} \frac{\partial I_2}{\partial y} \left( \frac{\partial u}{\partial y} + \frac{\partial v}{\partial x} \right) \tag{A.2}$$

$$G_2 = \frac{\partial I_2}{\partial y} \frac{\partial v}{\partial y} + \frac{1}{2} \frac{\partial I_2}{\partial x} \left( \frac{\partial u}{\partial y} + \frac{\partial v}{\partial x} \right) \tag{A.3}$$

$$I_2 = 2 \left( \frac{\partial u}{\partial x} \right)^2 + 2 \left( \frac{\partial v}{\partial y} \right)^2 + \left( \frac{\partial u}{\partial y} + \frac{\partial v}{\partial x} \right)^2 \tag{A.4}$$

If we put the next curvilinear expressions into necessary derivatives we will automatically get the curvilinear form of the equations.

$$u_x = u_\xi \xi_x + u_\eta \eta_x \tag{A.5}$$

$$u_y = u_\xi \xi_y + u_\eta \eta_y \quad (\text{A.6})$$

$$u_{xx} = u_{\xi\xi} \xi_x^2 + u_{\eta\eta} \eta_x^2 + u_{\xi\eta} \xi_x \eta_x + u_\eta \eta_{xx} + u_\xi \xi_{xx} \quad (\text{A.7})$$

$$u_{yy} = u_{\xi\xi} \xi_y^2 + u_{\eta\eta} \eta_y^2 + u_{\xi\eta} \xi_y \eta_y + u_\eta \eta_{yy} + u_\xi \xi_{yy} \quad (\text{A.8})$$

$$u_{xy} = u_{\xi\xi} \xi_x \xi_y + u_{\eta\eta} \eta_x \eta_y + u_{\xi\eta} (\eta_x \xi_y + \xi_x \eta_y) + u_\eta \eta_{xy} + u_\xi \xi_{xy} \quad (\text{A.9})$$

$$\begin{aligned} u_{xxx} = & (3u_{\xi\xi} \xi_x + u_{\xi\eta} \eta_x) \xi_{xx} + u_\xi \xi_{xxx} + (3u_{\eta\eta} \eta_x + u_{\xi\eta} \xi_x) \eta_{xx} + u_\eta \eta_{xxx} \\ & + (u_{\xi\xi\xi} \xi_x + u_{\xi\xi\eta} \eta_x) \xi_x^2 + (u_{\eta\eta\eta} \eta_x + u_{\eta\xi\eta} \eta_x) \eta_x^2 \\ & + 2(u_{\eta\xi\xi} \xi_x + u_{\eta\eta\xi} \eta_x) (\eta_x \xi_x) + 2u_{\xi\eta} (\eta_{xx} \xi_x + \eta_x \xi_{xx}) \end{aligned} \quad (\text{A.10})$$

$$\begin{aligned} u_{yyy} = & (3u_{\xi\xi} \xi_y + u_{\xi\eta} \eta_y) \xi_{yy} + u_\xi \xi_{yyy} + (3u_{\eta\eta} \eta_y + u_{\xi\eta} \xi_y) \eta_{yy} + u_\eta \eta_{yyy} \\ & + (u_{\xi\xi\xi} \xi_y + u_{\xi\xi\eta} \eta_y) \xi_y^2 + (u_{\eta\eta\eta} \eta_y + u_{\eta\xi\eta} \eta_y) \eta_y^2 \\ & + 2(u_{\eta\xi\xi} \xi_y + u_{\eta\eta\xi} \eta_y) (\eta_y \xi_y) + 2u_{\xi\eta} (\eta_{yy} \xi_y + \eta_y \xi_{yy}) \end{aligned} \quad (\text{A.11})$$

$$\begin{aligned} u_{xxy} = & (u_{\xi\xi} \xi_x + u_{\xi\eta} \eta_x) \xi_{xy} + u_\xi \xi_{xxy} + (u_{\eta\eta} \eta_x + u_{\xi\eta} \xi_x) \eta_{xy} + u_\eta \eta_{xxy} \\ & + (u_{\xi\xi\xi} \xi_x + u_{\xi\xi\eta} \eta_x) \xi_x \xi_y + u_{\xi\xi} (\xi_{xx} \xi_y + \xi_x \xi_{xy}) + (u_{\xi\eta\eta} \eta_x + u_{\xi\eta\xi} \xi_x) \eta_x \eta_y \\ & + u_{\eta\eta} (\eta_{xx} \eta_y + \eta_x \eta_{xy}) + (u_{\xi\xi\eta} \xi_x + u_{\xi\eta\eta} \eta_x) (\eta_x \xi_y + \eta_y \xi_x) \\ & + u_{\xi\eta} (\eta_{xx} \xi_y + \eta_x \xi_{xy} + \eta_{xy} \xi_x + \eta_y \xi_{xx}) \end{aligned} \quad (\text{A.12})$$

$$\begin{aligned}
u_{xyy} = & (u_{\xi\xi}\xi_y + u_{\xi\eta}\eta_y) \xi_{xy} + u_{\xi}\xi_{xyy} + (u_{\eta\eta}\eta_y + u_{\xi\eta}\xi_y) \eta_{xy} + u_{\eta}\eta_{xyy} \\
& + (u_{\xi\xi\xi}\xi_y + u_{\xi\xi\eta}\eta_y) \xi_x \xi_y + u_{\xi\xi} (\xi_{yy}\xi_x + \xi_y \xi_{xy}) + (u_{\xi\eta\eta}\eta_y + u_{\xi\eta\xi}\xi_y) \eta_x \eta_y \\
& + u_{\eta\eta} (\eta_{yy}\eta_x + \eta_y \eta_{xy}) + (u_{\xi\xi\eta}\xi_y + u_{\xi\eta\eta}\eta_y) (\eta_x \xi_y + \eta_y \xi_x) \\
& + u_{\xi\eta} (\eta_{yy}\xi_x + \eta_y \xi_{xy} + \eta_{xy}\xi_y + \eta_x \xi_{yy})
\end{aligned} \tag{A.13}$$

$$v_x = v_{\xi}\xi_x + v_{\eta}\eta_x \tag{A.14}$$

$$v_y = v_{\xi}\xi_y + v_{\eta}\eta_y \tag{A.15}$$

$$v_{xx} = v_{\xi\xi}\xi_x^2 + v_{\eta\eta}\eta_x^2 + v_{\xi\eta}\xi_x \eta_x + v_{\eta}\eta_{xx} + v_{\xi}\xi_{xx} \tag{A.16}$$

$$v_{yy} = v_{\xi\xi}\xi_y^2 + v_{\eta\eta}\eta_y^2 + v_{\xi\eta}\xi_y \eta_y + v_{\eta}\eta_{yy} + v_{\xi}\xi_{yy} \tag{A.17}$$

$$v_{xy} = v_{\xi\xi}\xi_x \xi_y + v_{\eta\eta}\eta_x \eta_y + v_{\xi\eta} (\eta_x \xi_y + \xi_x \eta_y) + v_{\eta}\eta_{xy} + v_{\xi}\xi_{xy} \tag{A.18}$$

$$\begin{aligned}
v_{xxx} = & (3v_{\xi\xi}\xi_x + v_{\xi\eta}\eta_x) \xi_{xx} + v_{\xi}\xi_{xxx} + (3v_{\eta\eta}\eta_x + v_{\xi\eta}\xi_x) \eta_{xx} + v_{\eta}\eta_{xxx} \\
& + (v_{\xi\xi\xi}\xi_x + v_{\xi\xi\eta}\eta_x) \xi_x^2 + (v_{\eta\eta\eta}\eta_x + v_{\eta\eta\xi}\xi_x) \eta_x^2 \\
& + 2(v_{\eta\xi\xi}\xi_x + v_{\eta\eta\xi}\eta_x) (\eta_x \xi_x) + 2v_{\xi\eta} (\eta_{xx}\xi_x + \eta_x \xi_{xx})
\end{aligned} \tag{A.19}$$

$$\begin{aligned}
v_{yyy} = & (3v_{\xi\xi}\xi_y + v_{\xi\eta}\eta_y) \xi_{yy} + v_{\xi}\xi_{yyy} + (3v_{\eta\eta}\eta_y + v_{\xi\eta}\xi_y) \eta_{yy} + v_{\eta}\eta_{yyy} \\
& + (v_{\xi\xi\xi}\xi_y + v_{\xi\xi\eta}\eta_y) \xi_y^2 + (v_{\eta\eta\eta}\eta_y + v_{\eta\eta\xi}\xi_y) \eta_y^2 \\
& + 2(v_{\eta\xi\xi}\xi_y + v_{\eta\eta\xi}\eta_y) (\eta_y \xi_y) + 2v_{\xi\eta} (\eta_{yy}\xi_y + \eta_y \xi_{yy})
\end{aligned} \tag{A.20}$$

$$\begin{aligned}
v_{xxy} = & (v_{\xi\xi}\xi_x + v_{\xi\eta}\eta_x) \xi_{xy} + v_{\xi}\xi_{xxy} + (v_{\eta\eta}\eta_x + v_{\xi\eta}\xi_x) \eta_{xy} + v_{\eta}\eta_{xxy} \\
& + (v_{\xi\xi\xi}\xi_x + v_{\xi\xi\eta}\eta_x) \xi_x \xi_y + v_{\xi\xi} (\xi_{xx}\xi_y + \xi_x \xi_{xy}) + (v_{\xi\eta\eta}\eta_x + v_{\xi\eta\xi}\xi_x) \eta_x \eta_y \\
& + v_{\eta\eta} (\eta_{xx}\eta_y + \eta_x \eta_{xy}) + (v_{\xi\xi\eta}\xi_x + v_{\xi\eta\eta}\eta_x) (\eta_x \xi_y + \eta_y \xi_x) \\
& + v_{\xi\eta} (\eta_{xx}\xi_y + \eta_x \xi_{xy} + \eta_{xy}\xi_x + \eta_y \xi_{xx})
\end{aligned} \tag{A.21}$$

$$\begin{aligned}
v_{xyy} = & (v_{\xi\xi}\xi_y + v_{\xi\eta}\eta_y) \xi_{xy} + v_{\xi}\xi_{xyy} + (v_{\eta\eta}\eta_y + v_{\xi\eta}\xi_y) \eta_{xy} + v_{\eta}\eta_{xyy} \\
& + (v_{\xi\xi\xi}\xi_y + v_{\xi\xi\eta}\eta_y) \xi_x \xi_y + v_{\xi\xi} (\xi_{yy}\xi_x + \xi_y \xi_{xy}) + (v_{\xi\eta\eta}\eta_y + v_{\xi\eta\xi}\xi_y) \eta_x \eta_y \\
& + v_{\eta\eta} (\eta_{yy}\eta_x + \eta_y \eta_{xy}) + (v_{\xi\xi\eta}\xi_y + v_{\xi\eta\eta}\eta_y) (\eta_x \xi_y + \eta_y \xi_x) \\
& + v_{\xi\eta} (\eta_{yy}\xi_x + \eta_y \xi_{xy} + \eta_{xy}\xi_y + \eta_x \xi_{yy})
\end{aligned} \tag{A.22}$$

where the subscripts indicate the partial derivatives.

## REFERENCES

1. Payver, P., “Laminar Heat Transfer in the Oil Groove of a Wet Clutch”, *International Journal of Heat Mass Transfer*, Vol. 34, pp. 1791–1798, 1991.
2. Burggraf, O. R., “Analytical and Numerical Studies of the Structure of Steady Separated Flows” *Journal of Fluid Mechanics*, Vol. 24 no. 1, pp. 113–151, 1966.
3. Botella, O. and R. Peyret, “Benchmark Spectral Results on the Lid-Driven Cavity Flow”, *Computers and Fluids*, Vol. 27, pp. 421–433, 1998.
4. Sahin, M. and R. G. Owens, “A Novel Fully Implicit Finite Volume Method Applied to the Lid-Driven Cavity Problem: Part:I. High Reynolds Number Flow Calculations”, *International Journal for Numerical Methods in Fluids*, Vol. 42, no. 42, pp. 57–77, 2003.
5. Gupta, M. M. and J. C. Kalita, “A new Paradigm for Solving Navier-Stokes Equations: Streamfunction–Velocity Formulation”, *Journal of Computational Physics*, Vol. 207, pp. 52–68, 2005.
6. Bruneau, C. H. and C. Jouron, “An Efficient Scheme for Solving Steady Incompressible Navier-Stokes Equations”, *Journal of Computational Physics*, Vol. 89, pp. 389–413, 1990.
7. Barragy, E. and G. F. Carey, “Stream Function-Vorticity Driven Cavity Solutions Using  $p$  Finite Elements”, *Computers and Fluids*, Vol. 26, pp. 453–468, 1997.
8. Ghia, U., K. N. Ghia and C. T. Shin, “High Re–Solution for Incompressible Navier–Stokes Equations and a Multigrid Method”, *Journal of Computational Physics*, Vol. 48, pp. 387–411, 1982.

9. Rubin, S. G. and P. K. Khosla, “Navier-Stokes Calculations with a Coupled Strongly Implicit Method”, *Computers and Fluids*, Vol. 9 , pp. 163–180, 1981.
10. Theodossiou, V. M. and A. C. M. Sousa, “An Efficient Algorithm for Solving the Incompressible Fluid Flow Equations”, *International Journal for Numerical Methods in Fluids*, Vol. 6, pp. 557–572, 1986.
11. Berger, E. J. and F. Sadeghi, C. M. Krousgrill, “Finite Element Modelling of Engagement of Rough and Grooved Wet Clutches”, *Journal of Tribology*, Vol. 118, pp. 137-146, 1996.
12. Chang, M. H. and C. H. Cheng, “Prediction of Lid-Driven Flow and Heat Convection in an Arc-Shape Cavity”, *International Communication of Heat Mass Transfer.*, Vol. 26 no. 6, pp. 829–838, 1999.
13. Grillet, A. M., B. Yang, B. Khomami and E. S. G. Shaqfeh, “Modeling of Viscoelastic Lid-Driven Cavity Flow Using Finite Element Simulations”, *Journal of Non-Newtonian Fluid Mechanics*, Vol. 88, pp. 99–131, 1999.
14. Grillet, A. M., E. S. G. Shaqfeh and B. Khomami, “Observation of Elastic Instabilities in Lid-Driven Cavity Flows”, *International Communication of Heat Mass Transfer.*, Vol. 94, pp. 15–35, 2000.
15. Bell, B. C. and K. S. Surana, “ $p$ -Version Least Squares Finite Element Formulation for two Dimensional Incompressible, Non-Newtonian Isothermal and Non-Isothermal Fluid Flow”, *International Journal for Numerical Methods in Fluids*, Vol. 18, pp. 127–162, 1994.
16. Neofytou, P., “A 3rd Order Upwind Finite Volume Method for Generalized Newtonian Fluid Flows”, *Advances in Engineering Software*, Vol. 36 , pp. 664–680, 2005.

17. Hoffmann, K. A. and S. T. Chiang, 1993, "Computational Fluid Dynamics For Engineers Vol:1-2" *Wichita, Kansas : A Publication of Engineering Education System*.
18. Knupp, P. and S. Steinberg, 1994, "Fundamentals of Grid Generation", *CRC Press, Inc.*
19. D'Alessio, S. J. D. and J. P. Pascal, "Steady Flow of a Power-Law Fluid Past a Cylinder", *Acta Mechanica*, Vol. 117, pp. 87-100, 1996.
20. Vanka, S. P., "Block-Implicit Multigrid Solution of Navier-Stokes Equations in Primitive Variables", *Journal of Computational Physics*, Vol. 65, pp. 138-158, 1986.
21. Schreiber, R. and H. B. Keller, "Driven Cavity Flows by Efficient Numerical Techniques", *Journal of Computational Physics*, Vol. 49, pp. 310-333, 1983.
22. Hou, S., Q. Zou, S. Chen, G. Doolen and A. Cogley, "Simulation of Cavity Flows by the Lattice Boltzmann Method", *Journal of Computational Physics*, Vol. 118, pp. 329-347, 1995.
23. Tillmark, L. N., "Numerical and Experimental Study of Driven Flow in a Polar Cavity", *International Journal for Numerical Methods in Fluids*, Vol. 5, pp. 311-329, 1985.
24. Kim, S. W., "Control-Volume Based Navier-Stokes Equation Solver Valid at all Flow Velocities", *NASA Technical Memorandum 101488*, ICOMP-89-5, 1989.
25. William, H., 1992, "Numerical Recipes in FORTRAN : Ther Art of Scientific Computing", *Cambridge University Press*, 2nd edition.

26. Chen, C. L. and Chin H. C., “ Experimental and Numerical Study of Mixed Convection and Flow Pattern in a Lid-Driven Arc-Shape Cavity”, *Journal of Heat Mass Transfer*, Vol. 41, pp. 58–66, 2004.